

Supplementary Information

for

Vacancy induced microstrain in high-entropy alloy film for sustainable hydrogen production under universal pH conditions

Yiyuan Yang^a, Zhe Jia^{a*}, Qianqian Wang^a, Yujing Liu^b, Ligang Sun^{c*}, Bo Sun^a, Juan Kuang^a, Shoujun Dai^d, Jianguo He^d, Sida Liu^e, Lunbo Duan^f, Hongjian Tang^f, Lai-Chang Zhang^g, Jamie J. Kruzic^h, Jian Luⁱ, Baolong Shen^{a*}

^a*School of Materials Science and Engineering, Jiangsu Key Laboratory for Advanced Metallic Materials, Southeast University, Nanjing, 211189, China*

^b*Institute of Metals, College of Materials Science and Engineering, Changsha University of Science & Technology, Changsha, 410114, China*

^c*School of Science, Harbin Institute of Technology, Shenzhen, 518055, China*

^d*Aerospace Information Research Institute, Chinese Academy of Sciences, Beijing, 100094, China*

^e*Laboratory for Multiscale Mechanics and Medical Science, SV LAB, School of Aerospace Xi'an Jiaotong University, Xi'an, 710049, China*

^f*Key Laboratory of Energy Thermal Conversion and Control, Ministry of Education, School of Energy and Environment, Southeast University, Nanjing, 210096, China*

^g*Centre for Advanced Materials and Manufacturing, School of Engineering, Edith Cowan University, 270 Joondalup Drive, Joondalup, Perth, WA 6027, Australia*

^h*School of Mechanical and Manufacturing Engineering, University of New South Wales (UNSW Sydney), Sydney, NSW 2052, Australia*

ⁱ*Hong Kong Branch of National Precious Metals Material Engineering Research Center and Department of Mechanical Engineering, City University of Hong Kong, Hong Kong SAR, China*

Experimental Section

Materials

Fe (99.99 wt.%), Co (99.99 wt.%), Ni (99.99 wt.%), Cr (99.99 wt.%), and Pt (99.99 wt.%) granules were weighed and mixed to produce a high entropy alloy (HEA) with equal atomic composition of FeCoNiCrPt. Analytical grade potassium hydroxide (KOH) and sulfuric acid (H₂SO₄) were supplied by Aladdin (Shanghai, China), and absolute ethanol was supplied by Nanjing WANQING Chemical Glassware & Instrument Co., Ltd (Nanjing, China). Deionized water was used to dilute the KOH and H₂SO₄ solutions. IrO₂ was supplied by Macklin (Shanghai, China), and 20% Pt/C was supplied by Johnson Matthey (London, England).

Film preparation

The HEA films were prepared by laser pulsed deposition (PLD). Specifically, a master alloy ingot (~20 g) with equal atomic composition of FeCoNiCrPt was first prepared by arc-melting under high-purity argon (Ar) atmosphere with Ti-gettering to minimize oxidation. The ingot was remelted at least four times to ensure the homogeneity of metal elements. Afterwards, the master alloy ingot was cut into cylinder with dimensions of Φ 17 mm \times 2 mm as the target. The configuration of the PLD equipment is shown in Fig. 1a. The working argon pressure was 10⁻³ Pa. The substrate temperature was set at 300 K. The laser wavelength was 1064 nm. The deposition lasted for 15 min under argon protection to prepare the FeCoNiCrPt HEA film on carbon paper and commercial Ni foam substrates. The mass of the samples before and after deposition were acquired by a high-precision balance for the calculation of the mass activity. Next, the as-deposited (denoted as as-dep) HEA films were electrochemically etched at 0.98 V (vs. SCE) in a 0.5 M H₂SO₄ solution for different time intervals of 150, 300, and 800 seconds (denoted as EE.150s, EE.300s, and EE.800s, respectively). The treated films were then washed by deionized water and ethanol three times.

Materials characterization

Grazing incidence X-ray diffraction (GIXRD, Rigaku Smartlab 9 kw) analyses were

performed to determine the crystal structure of the HEA film. The surface morphology was investigated using a scanning electron microscope (SEM, Nova Nano SEM450), and the morphology after the stability test was characterized on a Zeiss Sigma 300 SEM. The microstructure was analyzed using a high-resolution transmission electron microscope (HRTEM, Talos F200X) coupled with selected area electron diffraction (SAED) and energy-dispersive spectrometry (EDS). Atomic-resolution scanning transmission electron microscopy (STEM) images and EDS mappings were acquired using a double spherical aberration corrected transmission electron microscope (AC-TEM, FEI-Themis Z). The AC-TEM specimen was prepared using an FEI focused ion beam/scanning electron microscope (FIB/SEM). Geometric phase analyses (GPA) were carried out using the GPA plug-in software for strain measurement in the Digital Micrograph software (Gatan). X-ray photoelectron spectroscopy (XPS) was conducted using a Thermo Scientific K-Alpha instrument. Inductively coupled plasma-optical emission spectrometry (ICP-OES) was used to quantify different element ratios of the films before and after electrochemical etching (Agilent 5110) as well as leached metallic ions after stability experiments (Spectro Blue).

Synchrotron-based X-ray absorption spectroscopy (XAS) was performed with Si (111) crystal monochromators at the Singapore Synchrotron Light Source (SSLS). Extended X-ray absorption fine structure (EXAFS) spectra were recorded in transmission mode. Negligible changes in the line-shape and peak position of Pt L_3 -edge XANES spectra were observed between two scans taken for a specific sample. Data reduction, data analysis, and EXAFS fitting were performed and analyzed with the Athena and Artemis programs of the Demeter data analysis packages¹ that uses the FEFF6 program² to fit the EXAFS data. The energy calibration of the sample was conducted adopting a standard Pt foil, which as a reference was simultaneously measured. A linear function was subtracted from the pre-edge region, and the edge jump was then normalized using Athena software. The $\chi(k)$ data were isolated by subtracting a smooth, third-order polynomial approximating the absorption background of an

isolated atom. The k^3 -weighted $\chi(k)$ data were Fourier transformed after applying a Hanning window function ($\Delta k = 1.0$). For EXAFS modelling, the global amplitude EXAFS (CN , R , σ^2 , and ΔE_0) was obtained by nonlinear fitting, with least-squares refinement, of the EXAFS equation to the Fourier-transformed data in R -space, using Artemis software, EXAFS of the Pt foil is fitted and the obtained amplitude reduction factor S_0^2 value (0.837) was set in the EXAFS analysis to determine the coordination numbers (CNs) on the Pt-C/O/Pt/M (M = Fe, Co, Ni, Cr) scattering path in sample. For wavelet transform analysis, the $\chi(k)$ exported from Athena was imported into the Hama Fortran code.³ The parameters used are listed as follows: R -range of 1-4.0 Å, k -range of 0-13.0 Å⁻¹ for the sample (and 0-13.0 Å⁻¹ for the Pt foil and PtO₂), and k weight of 2. A Morlet function with $\kappa = 8$ and $\sigma = 1$ was used as the mother wavelet to provide the overall distribution.

Electrochemical measurements

The electrochemical catalytic performance was conducted using a standard three-electrode electrochemical station (Gamry Interface 1000) under pH-universal conditions, including 1.0 M KOH, 0.5 M H₂SO₄, and 1.0 M phosphate buffered saline (PBS) electrolytes. A graphite rod was used as the counter electrode, a saturated calomel electrode (SCE) as the reference electrode, and the HEA film on the carbon paper as the freestanding working electrode. All potentials reported in this work were calibrated against reversible hydrogen electrode (RHE) according to: $E_{\text{RHE}} = E_{\text{SCE}} + 0.0591 \times \text{pH} + 0.2412$. All samples were activated by cyclic voltammetry until the performance was stable before electrochemical measurement. Linear sweep voltammetry (LSV) for HER was carried out at a scan rate of 5 mV s⁻¹ by iR compensation. The polarization curves were normalized by the geometric surface area. Pt wire ($\Phi 1 \times 37$ mm), Pt sheet (5×5 mm), and Pt/C (20 wt.%) catalysts were investigated for comparison. The Pt/C catalyst inks were loaded on a glass carbon electrode (0.07 cm²) with a mass loading of 0.17 mg cm⁻².

Electrochemical impedance spectroscopy (EIS) was carried out from 0.1 to 10⁵ Hz.

Double layer capacitance (C_{dl}) was determined by measuring a series of cyclic voltammograms (CVs) at sweep rates ranging from 10 to 50 mV s^{-1} in the non-faradaic potential region. The electrochemical surface areas (ECSAs) were calculated according to the equation of $\text{ECSA} = C_{dl}/C_s$, where C_s is the specific capacitance per unit area. In this work, C_s was chosen as 0.04 mF cm^{-2} for 1.0 M KOH. Chronoamperometry tests at static current densities of 10 and 100 mA cm^{-2} for the alkaline condition, and 10 mA cm^{-2} for the neutral and acidic conditions were conducted to evaluate the stability of the catalysts without iR loss correction.

Faradaic efficiency (FE) was measured using a drainage method at 25 °C at the currents of 25, 50, 100, 200, and 500 mA, and was calculated using the formula as follows,

$$\begin{aligned} \text{FE} &= \frac{2 \times \text{total number of hydrogen produced (mol)} \times \text{Faraday constant} \left(\frac{\text{C}}{\text{mol}} \right)}{\text{Quantity of electric charge (C)}} \\ &= \frac{2 \times \text{total number of hydrogen produced (mol)} \times \text{Faraday constant} \left(\frac{\text{C}}{\text{mol}} \right)}{\text{Current (A)} \times \text{time (s)}} \\ \text{Number of hydrogen turnovers} &= \frac{\text{volume of hydrogen produced (L)}}{\text{molar volume of gas (L/mol)}} \end{aligned}$$

The molar volume of gas is 24.8 L/mol at 25°C under standard atmospheric pressure.

For a flow-type anion exchange membrane (AEM) electrolyzer test, the EE.300s HEA film and IrO_2 were used as cathode and anode catalytic materials, respectively. S-type Ti current collectors with a serpentine flow field play the role of electric conduction and electrolyte transmission. As for the cathode/anode compartment, the AEM electrolyzer was assembled in the following sequence: end plate, sealing gasket, Ti current collector, EE.300s film on the Ni foam, anion-exchange membrane, IrO_2 , Ti current collector, and sealing gasket. The geometric area of the EE.300s film was 1.6 cm^2 . An anion-exchange membrane (Fumasep FAA-3-PK-130) was used to separate the cathode and anode compartments of the electrolyzer. During the tests, 1.0 M KOH electrolyte was fed to both sides of the electrolyzer at a rate of 2.5 ml min^{-1} under the control of a peristaltic pump. In addition, the Pt/C || IrO_2 system was also tested for

comparison. The Pt/C and IrO₂ catalyst inks were loaded on carbon papers (1.6 cm²) with a precious metal mass loading of 0.43 mg cm⁻² for both.

The turnover frequency (TOF) was calculated from the current density using the formula:⁴

$$\text{TOF} = \frac{\text{Total number of hydrogen turnovers per second}}{\text{Number of active sites}} = \frac{|j|\varepsilon A_{\text{geo}} N_A / (2F)}{A_{\text{ECSA}} / (v_a)^{2/3}}$$

where j is the geometric current density of the catalyst, ε is the Faradaic efficiency of the catalyst, A_{geo} is the geometric area of the catalyst material, A_{ECSA} is the electrochemically active surface area of the catalyst, s_a is the average area of each active site and can be calculated from the volume of each active site v_a via $s_a = (v_a)^{2/3}$, N_A is the Avogadro constant 6.022×10^{23} mol⁻¹, F is the Faraday constant 96485.3 C mol⁻¹, and the factor 2 is the mole number of electrons per mole H₂.

The parameters needed for the calculation of v_a are taken from the literature⁵ and shown in Table 1,

Table 1. The crystallographical information of five principal elements.

Element	Crystal structure	Lattice constant (nm)	Number of atoms in a unit cell	Atomic volume (nm ³)
Fe	BCC	a = b = c = 0.28665	2	0.01177
Co	HCP	a = b = 0.25071 c = 0.40695	6	0.011076
Ni	FCC	a = b = c = 0.3524	4	0.01094
Cr	BCC	a = b = c = 0.291	2	0.012321
Pt	FCC	a = b = c = 0.39236	4	0.0151

For the FeCoNiCrPt HEA film, we assumed that all surface Fe, Co, Ni, Cr, and Pt atomic sites are equally active because the actual active sites are unknown for the FeCoNiCrPt HEA film. This assumption would result in an overestimate of the number of active sites and thus an underestimate of the true TOF values. The average volume of each active site can be calculated using $v_a = f_{\text{Fe}} \times (v_a)_{\text{Fe}} + f_{\text{Co}} \times (v_a)_{\text{Co}} + f_{\text{Ni}} \times (v_a)_{\text{Ni}} + f_{\text{Cr}} \times (v_a)_{\text{Cr}} + f_{\text{Pt}} \times (v_a)_{\text{Pt}}$, where f is the atomic fraction in the FeCoNiCrPt HEA film. The TOF of FeCoNiCrPt HEA films can thus be calculated.

In-situ Raman measurements were carried out on a confocal microscope Raman system (WiTec Alpha300), using a 532-nm laser as the excitation source. The power of the laser was 17 mW. A homemade Raman cell was used to conduct the in situ electrochemical Raman experiments (Fig. S16).

Density functional theory simulations

Density functional theory (DFT) method was employed to conduct first-principle calculations about the HER process of FeCoNiCrPt HEA by using the Cambridge Sequential Total Energy Package (CASTEP) module in Materials Studio software.⁶ Generalized gradient approximation method with the Perdew-Burke-Ernzerh function (GGA-PBE) was adopted to describe the exchange and corrections of atomic interaction.⁷ The interactions between valence electrons and ionic cores was described by ultrasoft pseudo-potential method.⁸ A plane-wave basis set with a cutoff energy of 400 eV was assigned. The Brillouin zone was sampled by a Monkhorst-Pack grid.⁹ The tolerances of energy, force and displacement first-principles calculations are 10^{-5} eV/atom, 0.03 eV/Å, and 0.002 Å, respectively. The self-consistence field (SCF) was set as 1×10^{-5} eV/atom.

The water adsorption energies at the active sites of catalysts were calculated as $E_{\text{H}_2\text{O}} = E_{\text{surf}+\text{H}_2\text{O}} - E_{\text{surf}} - E_{\text{H}_2\text{O}}$, where E_{surf} and $E_{\text{surf}+\text{H}_2\text{O}}$ are the total energies of the catalyst surface before and after water adsorption onto the active sites, and $E_{\text{H}_2\text{O}}$ is the energy of a free water molecule. The Gibbs free energies for hydrogen adsorption were calculated according to $\Delta G_{\text{H}^*} = \Delta E_{\text{H}^*} + \Delta \text{ZPE} - T\Delta S$, where the ΔE_{H^*} , ΔZPE , T and ΔS are the binding energy, zero-point energy change, temperature and entropy change of H adsorption system, respectively. Generally, the vibration entropy of H at the adsorbed states is negligible. ΔS was thus obtained as $\Delta S = S_{\text{H}^*} - \frac{1}{2}S_{\text{H}_2} \approx -\frac{1}{2}S_{\text{H}_2}$, where S_{H_2} is the entropy of H_2 in the gas phase under the standard conditions. ΔZPE was calculated according to $\Delta \text{ZPE} = \text{ZPE}_{\text{H}^*} - \frac{1}{2}\text{ZPE}_{\text{H}_2}$. Therefore, the free energy of the adsorbed state of H (H^*) was calculated using the simplified equation

$$\Delta G_{\text{H}^*} = \Delta E_{\text{H}^*} + 0.24 \text{ eV}.$$

According to the results from experimental analyses, the main characteristics of EE.300s etched sample that differ from the as-dep ones were the composition, microstrain, and vacancies. Two kinds of representative face-centered cubic FeCoNiCrPt atomistic models, with similar compositions and conditions similar to those of the samples in our experiment, were constructed to investigate the HER performance; i.e., a) an as-deposited model (referred to as the “as-dep” model) and b) a model etched for 300 s with microstrain and vacancies (referred to as the “EE.300s” model). Structure optimizations were performed for these models to determine the crystal structure, with k points set as $(3 \times 3 \times 2)$. The (111) surfaces were then cleaved from the optimized periodic structures with a vacuum layer of $\sim 15 \text{ \AA}$. These surface models were further geometrically optimized and utilized to study the effect of composition, microstrain, and vacancies on the HER performance of FeCoNiCrPt, with k points set as $(3 \times 3 \times 1)$.

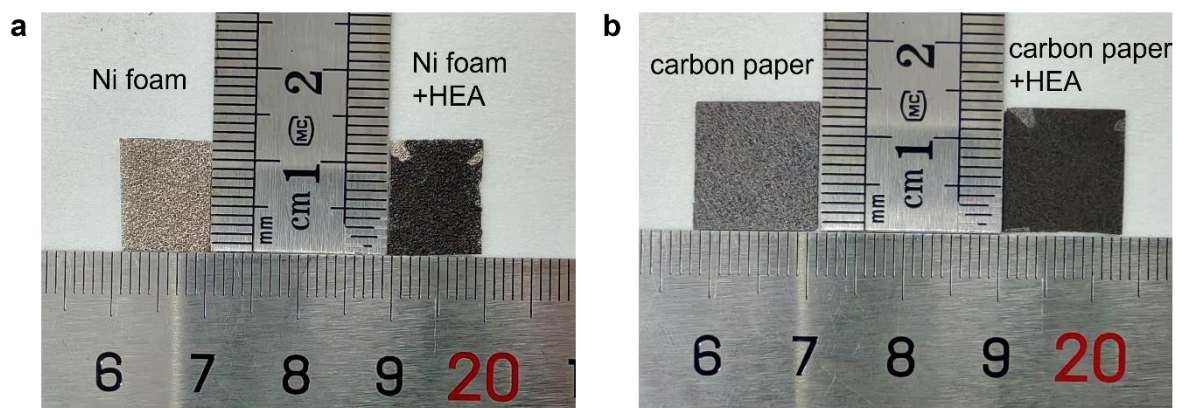


Figure S1. Photographs of the substrates before and after the FeCoNiCrPt HEA films were deposited on them. (a) Ni foam (left) and the FeCoNiCrPt HEA film deposited on it (right). (b) Carbon paper (left) and the FeCoNiCrPt HEA film deposited on it (right).

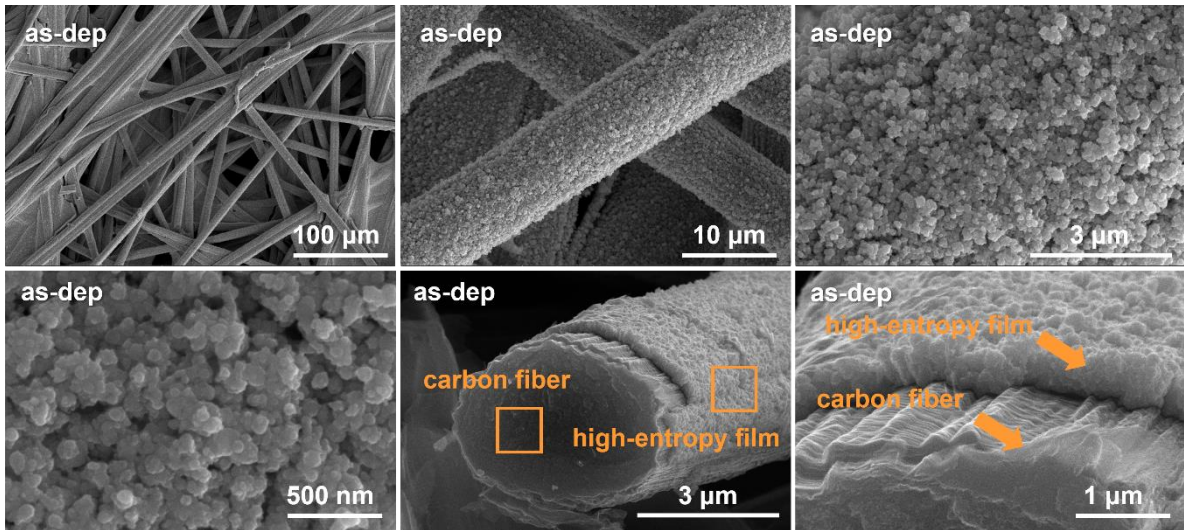


Figure S2. Scanning electron microscopy characterization. SEM images of the as-dep FeCoNiCrPt HEA film deposited on carbon paper under various magnifications.

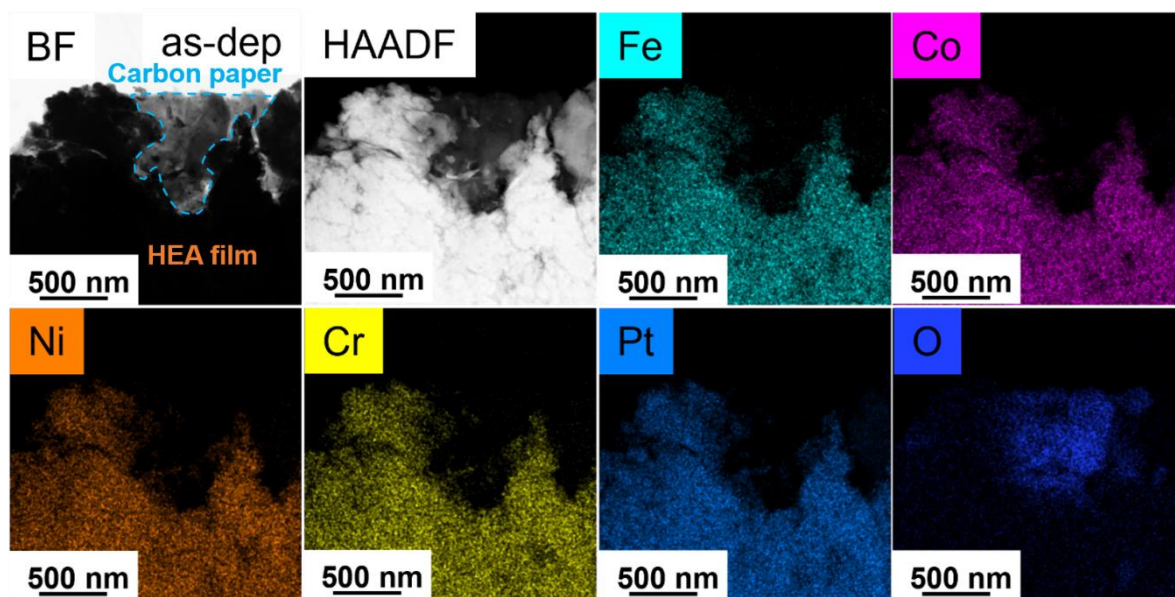


Figure S3. Elemental investigation. EDS mapping of the as-dep FeCoNiCrPt HEA film.

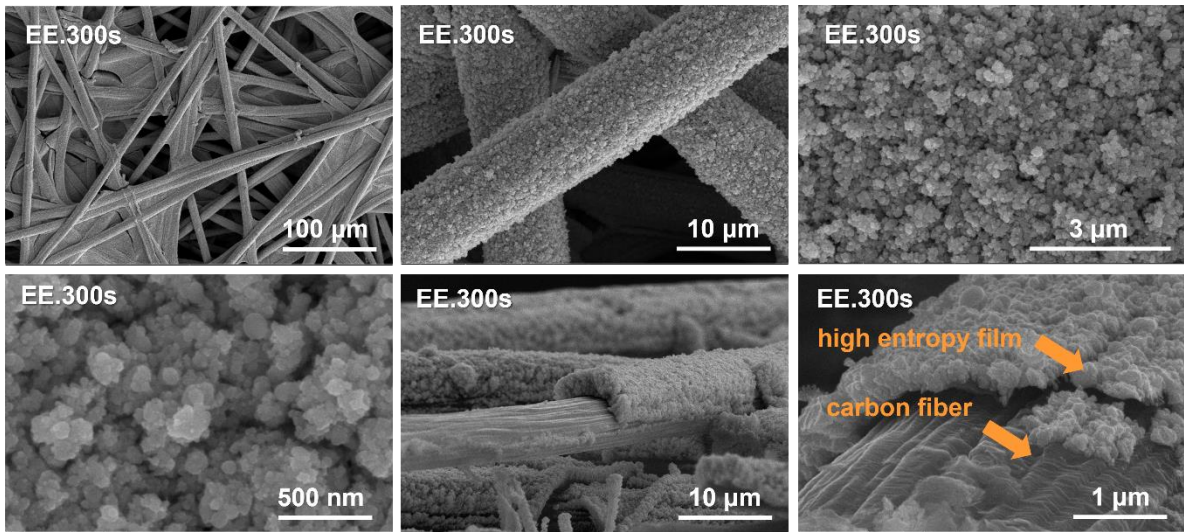


Figure S4. Scanning electron microscopy characterization. SEM images of the EE.300s FeCoNiCrPt HEA film under various magnifications.

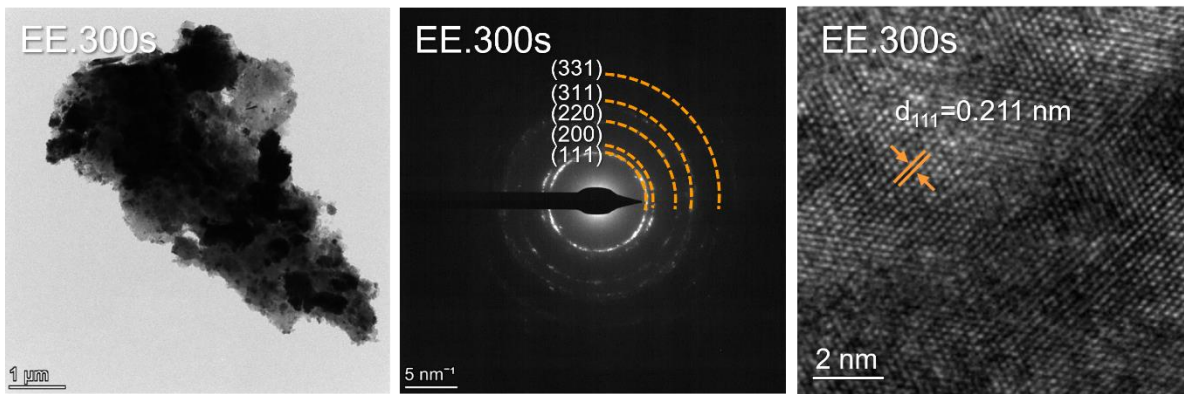


Figure S5. Transmission electron microscopy characterization. (a) TEM image (b) SAED pattern, and (c) HRTEM image of the EE.300s film.

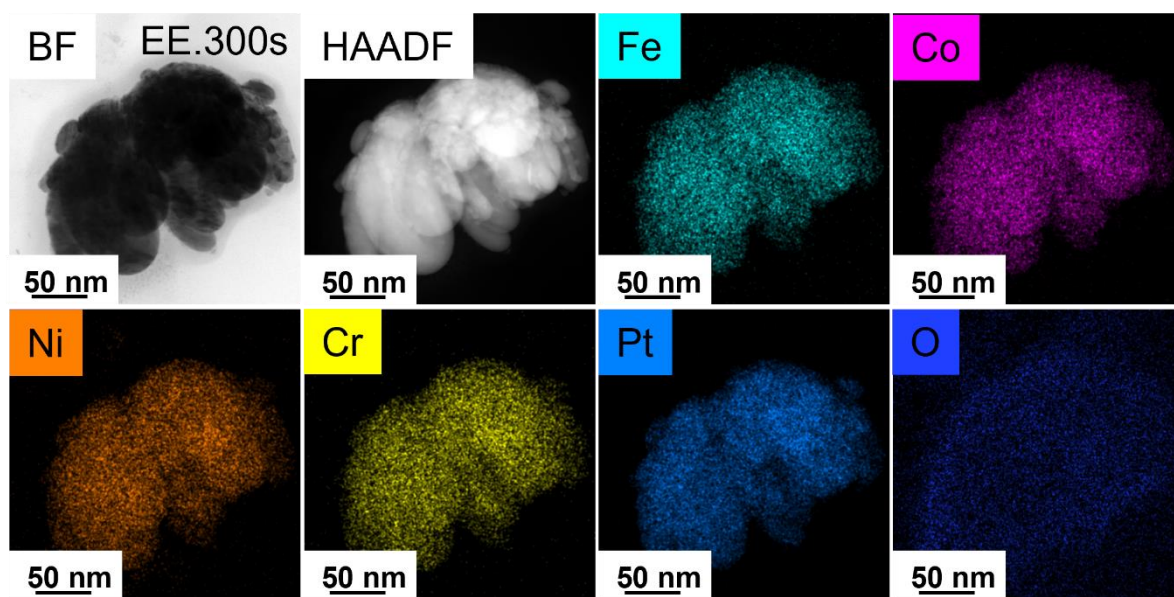


Figure S6. Elemental investigation. EDS mapping of the EE.300s film.

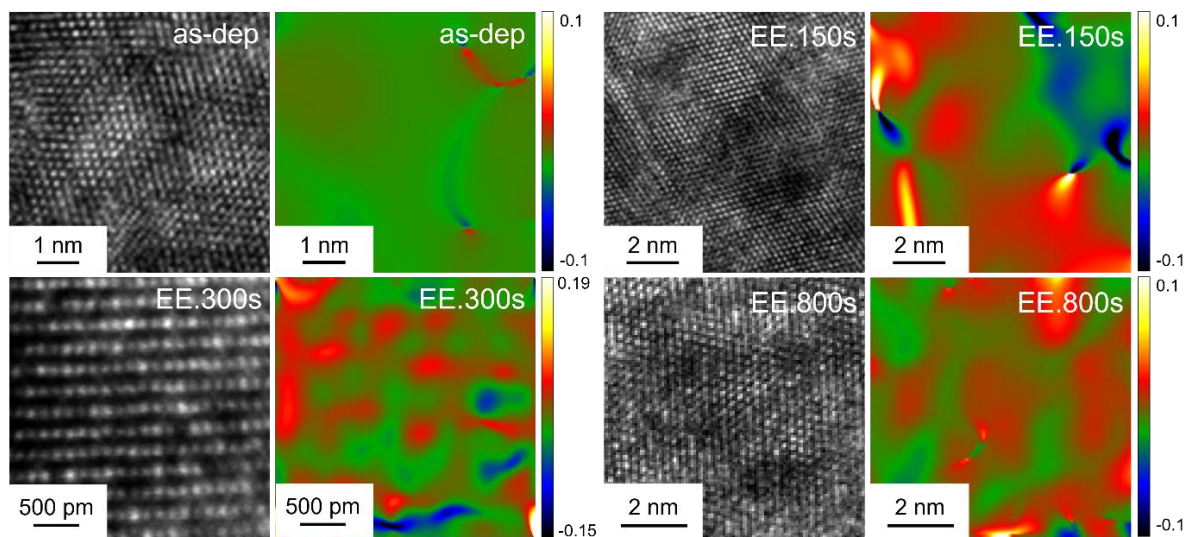


Figure S7. Microstrain characterization of the FeCoNiCrPt HEA films. Lattice-resolution TEM and GPA images used for normal strain (ϵ_{xx}) analysis of (a) as-dep, (b) EE.150s, (c) EE.300s, and (d) EE.800s films.

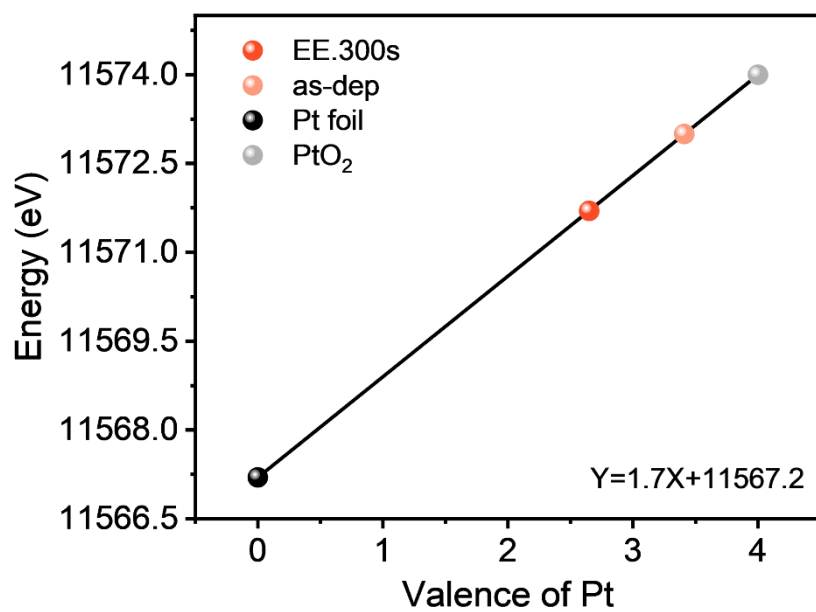


Figure S8. Pt L_3 -edge energies for Pt foil, PtO₂, as-dep, and EE.300s films as a function of the Pt valence.

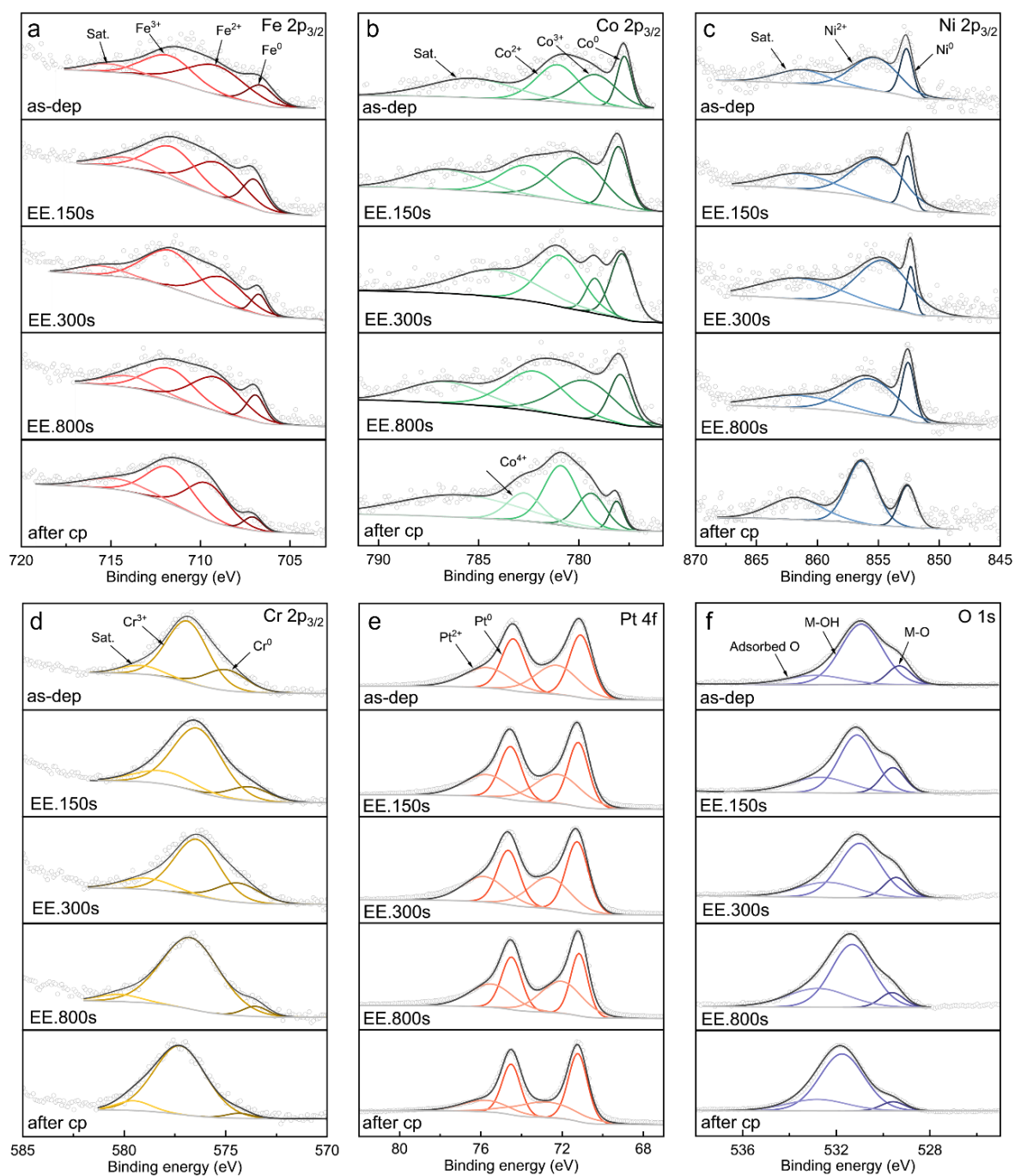


Figure S9. XPS spectra of (a) Fe, (b) Co, (c) Ni, (d) Cr, (e) Pt, and (f) O for as-dep, EE.150s, EE.300s, EE.800s films, and the EE.300s film after chronoamperometry testing.

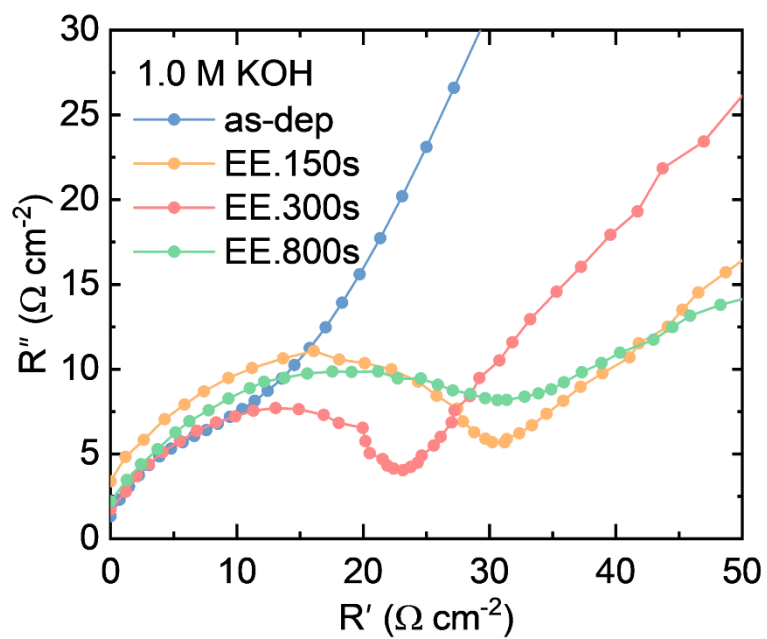


Figure S10. Electrochemical impedance spectroscopy analysis. Nyquist plots of the HEA films in 1.0 M KOH.

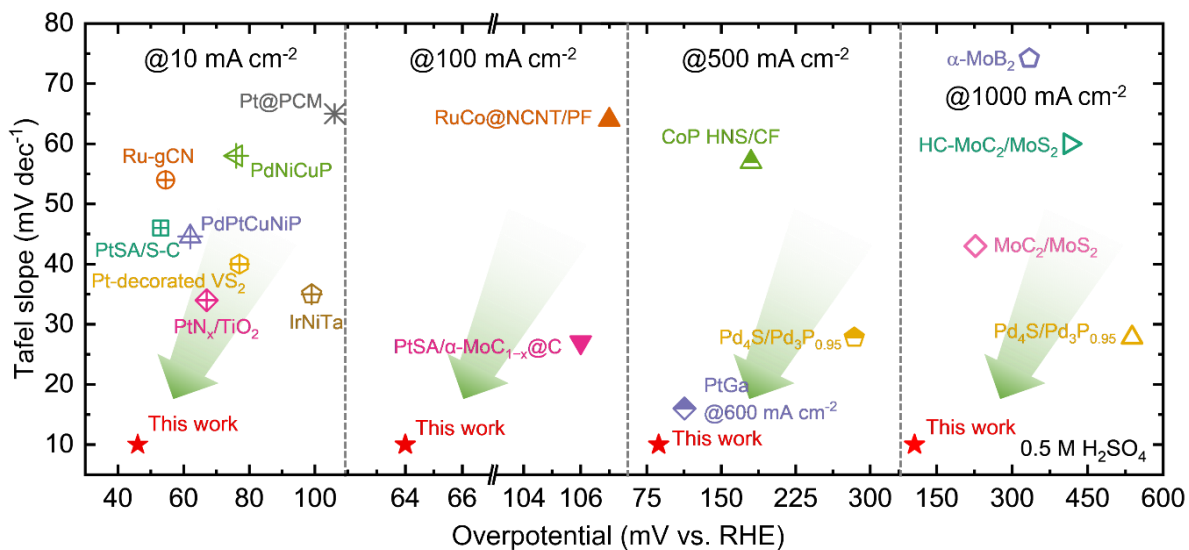


Figure S11. Performance comparison. Comparison of acidic HER activities with recently reported electrocatalysts at current densities of 10, 100, 500, and 1000 mA cm⁻² in 0.5 M H₂SO₄.

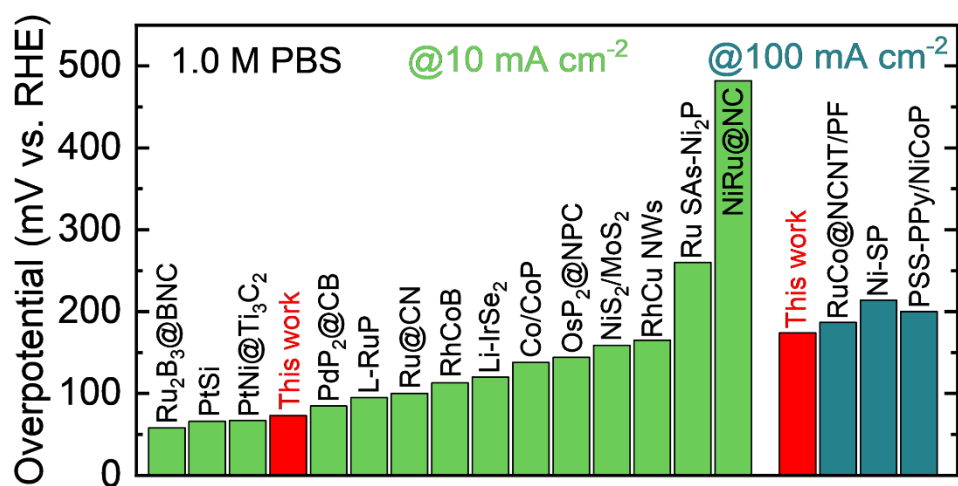


Figure S12. Comparison of neutral HER activities with recently reported electrocatalysts at current densities of 10, 100 mA cm⁻² in 1.0 M PBS.

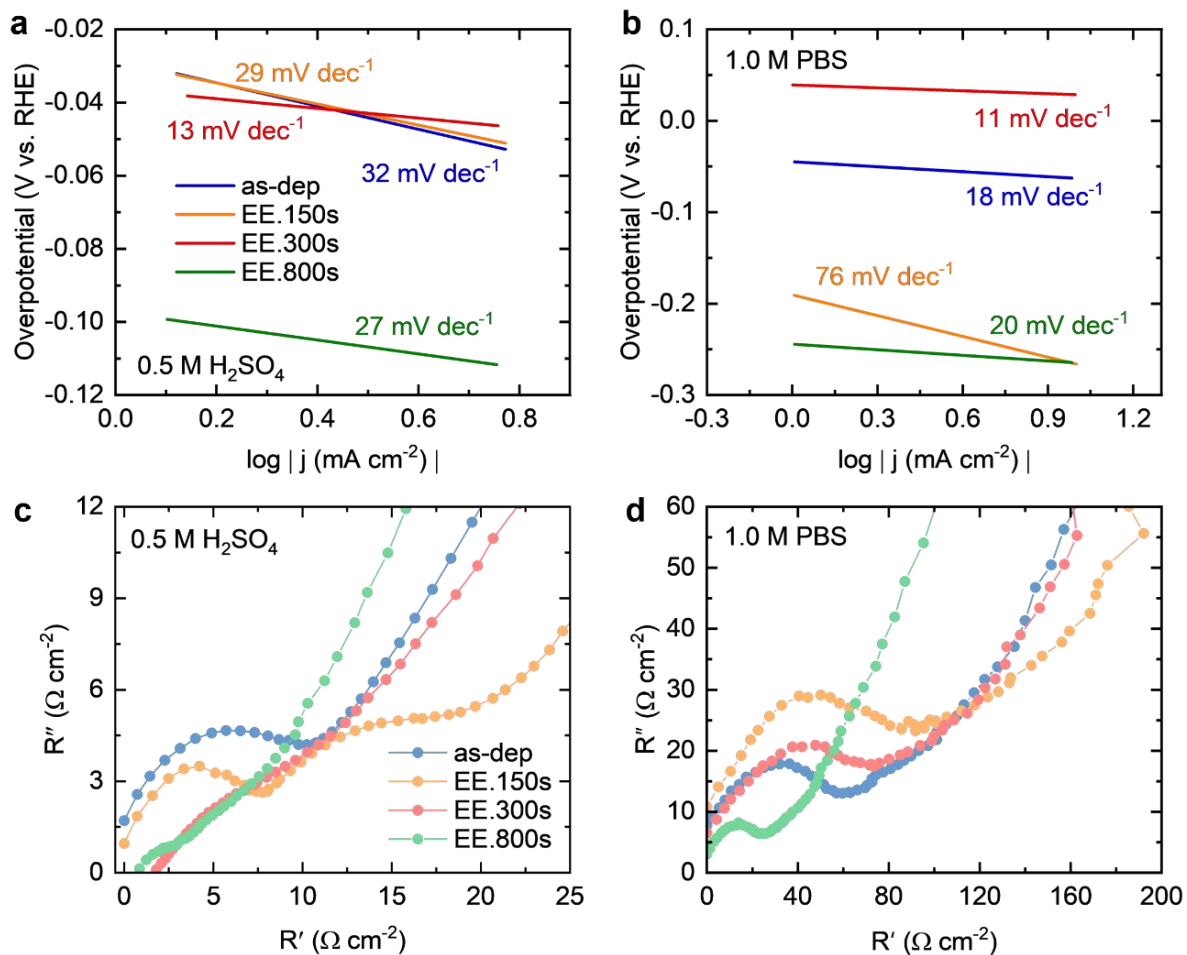


Figure S13. The kinetic analysis of HER in 0.5 M H₂SO₄ and 1.0 M PBS solutions. (a,b) Tafel plots derived from the polarization curves. (c,d) Nyquist plots analyzed by EIS.

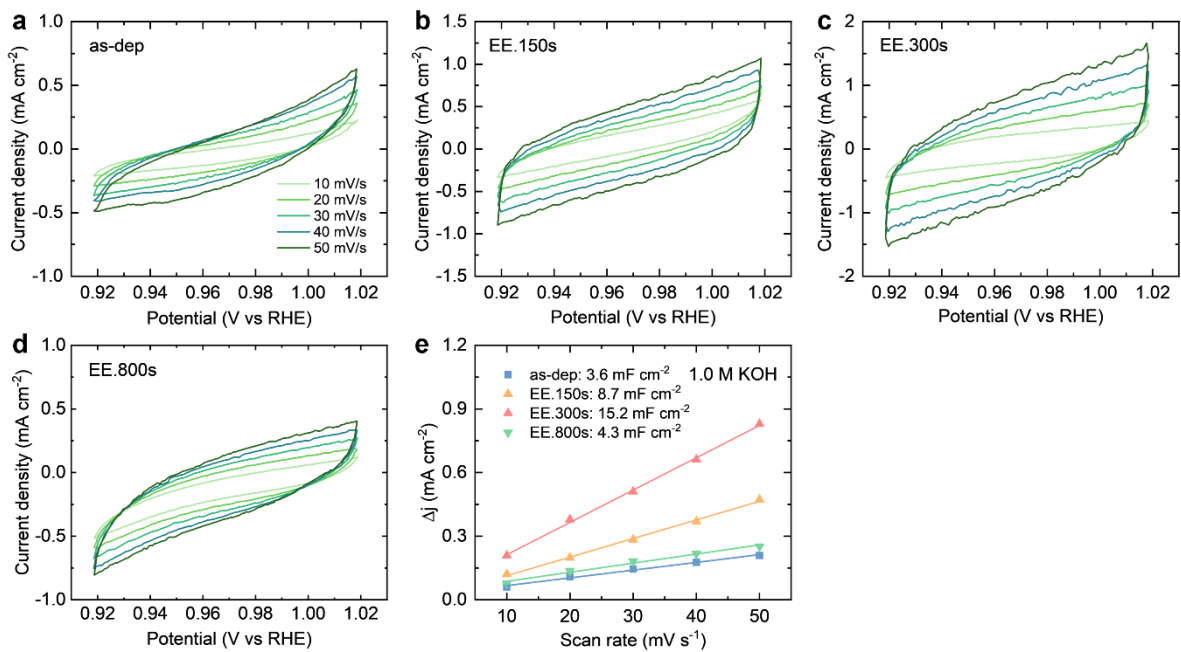


Figure S14. Electrochemical active surface area analysis. Cyclic voltammery curves at scan rates of 10, 20, 30, 40, and 50 mV s^{-1} for (a) as-dep, (b) EE.150s, (c) EE.300s, and (d) EE.800s films. (e) The capacitive currents plotted for the HEA films.

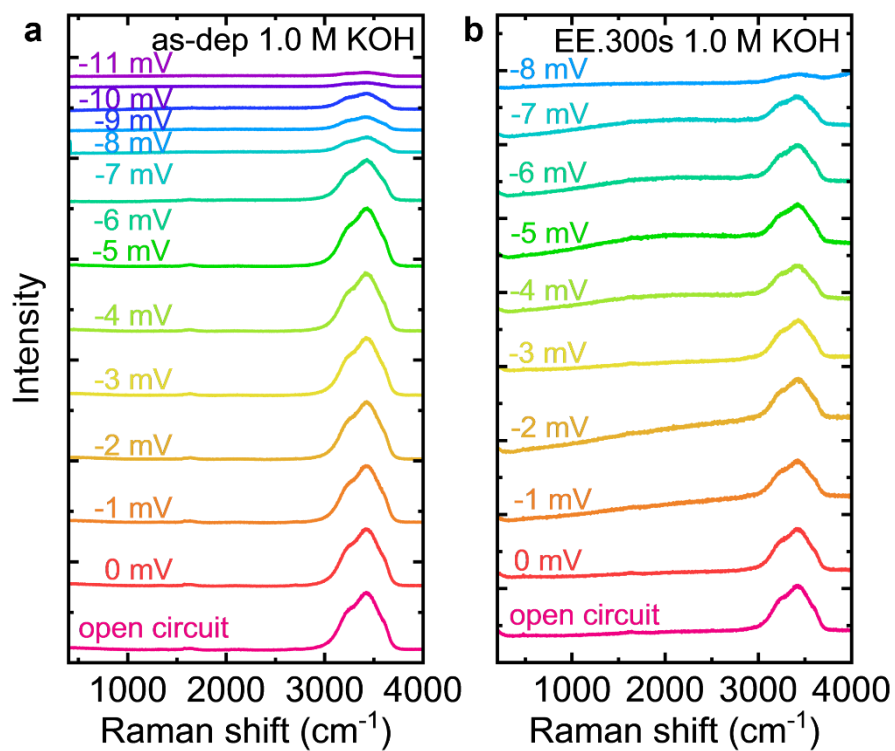


Figure S15. In-situ Raman analysis. The operando Raman spectra of (a) as-dep and (b) EE.300s films in 1.0 M KOH.

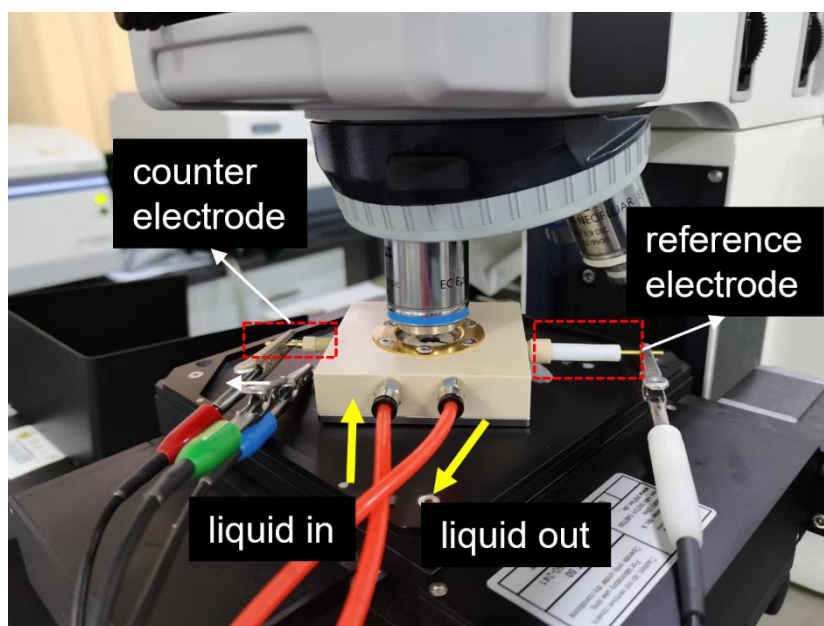


Figure S16. In-situ Raman characterization platform.

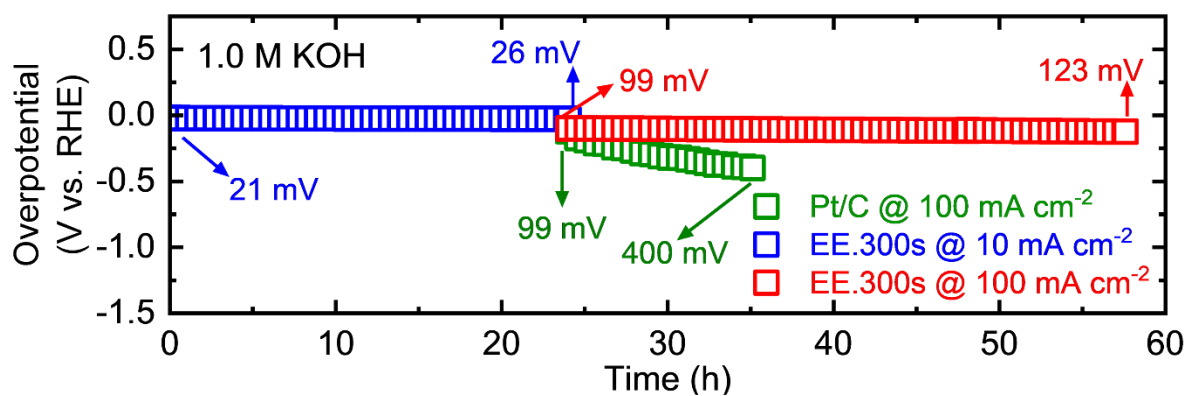


Figure S17. Chronopotentiometry curves of EE.300s film for HER at current densities of 10 and 100 mA cm⁻², as well as Pt/C at a current density of 100 mA cm⁻² in 1.0 M KOH without *iR* loss correction.

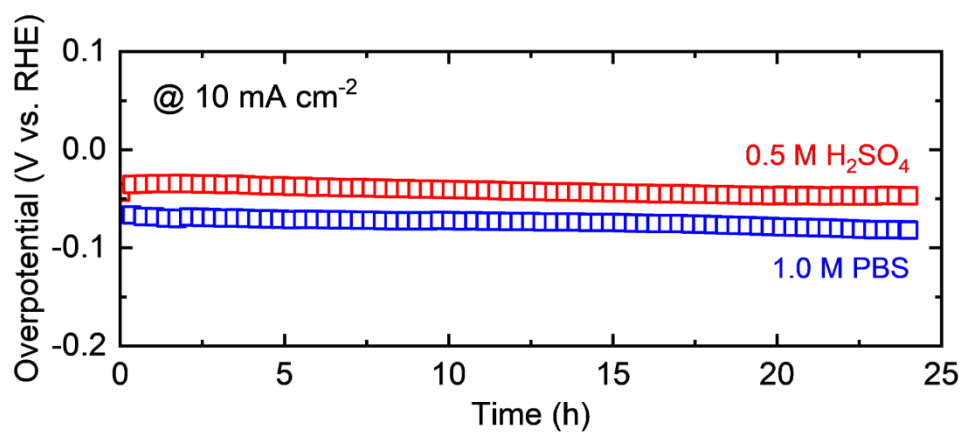


Figure S18. Chronopotentiometry curves of EE.300s film at a current density of 10 mA cm⁻² in 0.5 M H₂SO₄ and 1.0 M PBS solutions without *iR* loss correction.

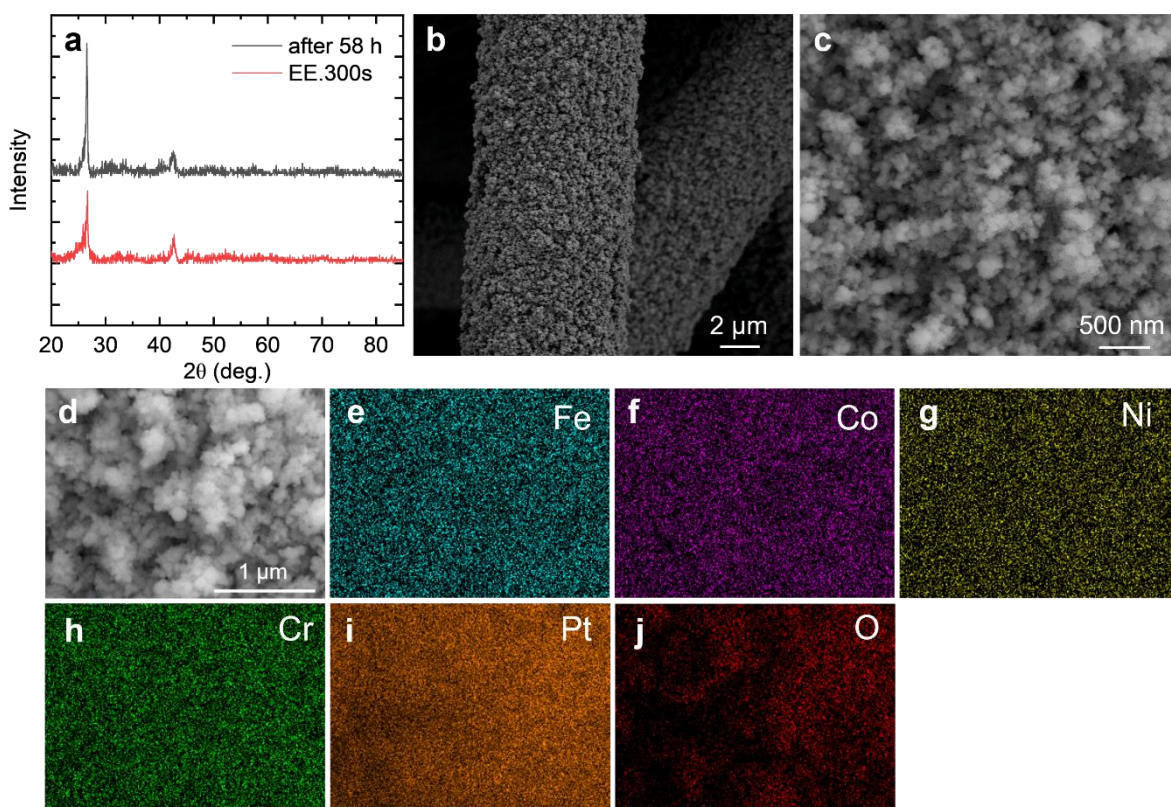


Figure S19. Characterization of EE.300s film after durability testing in 1.0 M KOH for 58 h. (a) GIXRD data of the used EE.300s film. (b-d) SEM images of the used EE.300s film under different magnifications. (e-j) EDS mappings of the used EE.300s film.

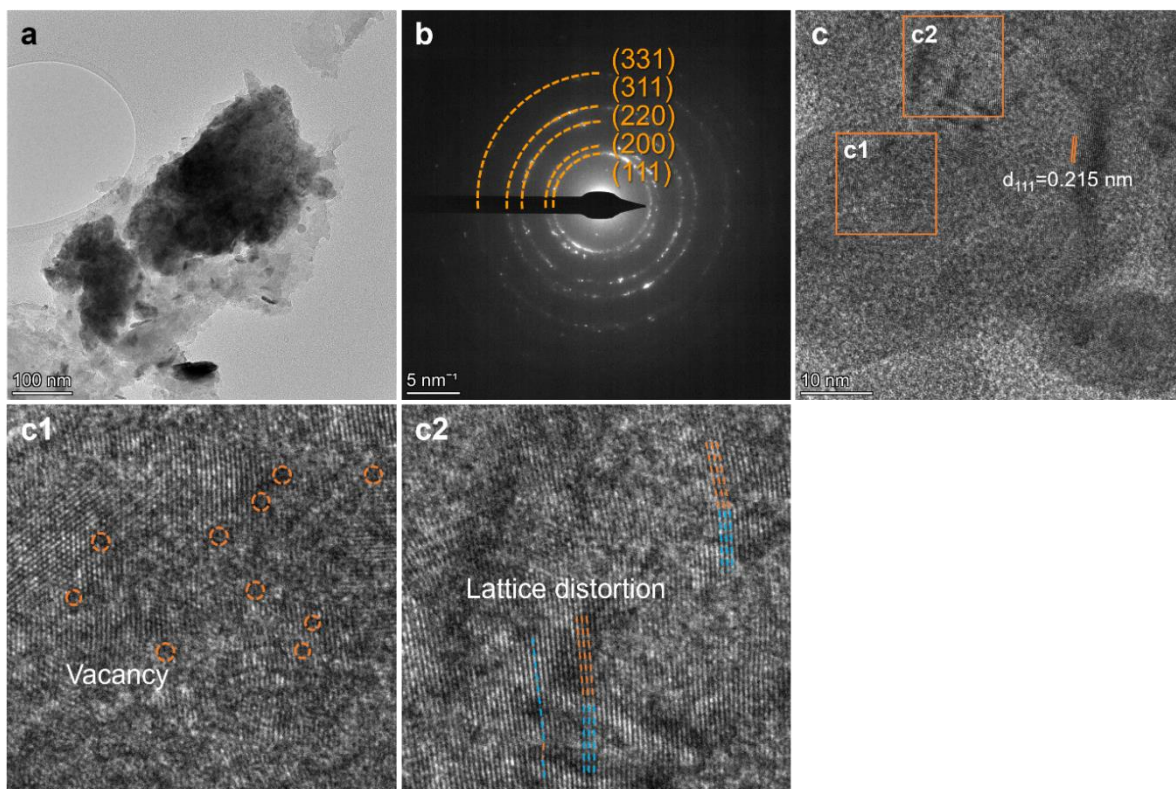


Figure S20. Transmission electron microscopy investigation of the used EE.300s film after 58 h of HER durability test in 1.0 M KOH. (a) TEM image and (b) corresponding SAED pattern of the used EE.300s film. (c) HRTEM image of the used EE.300s film. (c1) Close-up map of the representative area with high density of vacancies in (c). (c2) Close-up map of the representative area with lattice distortion in (c).

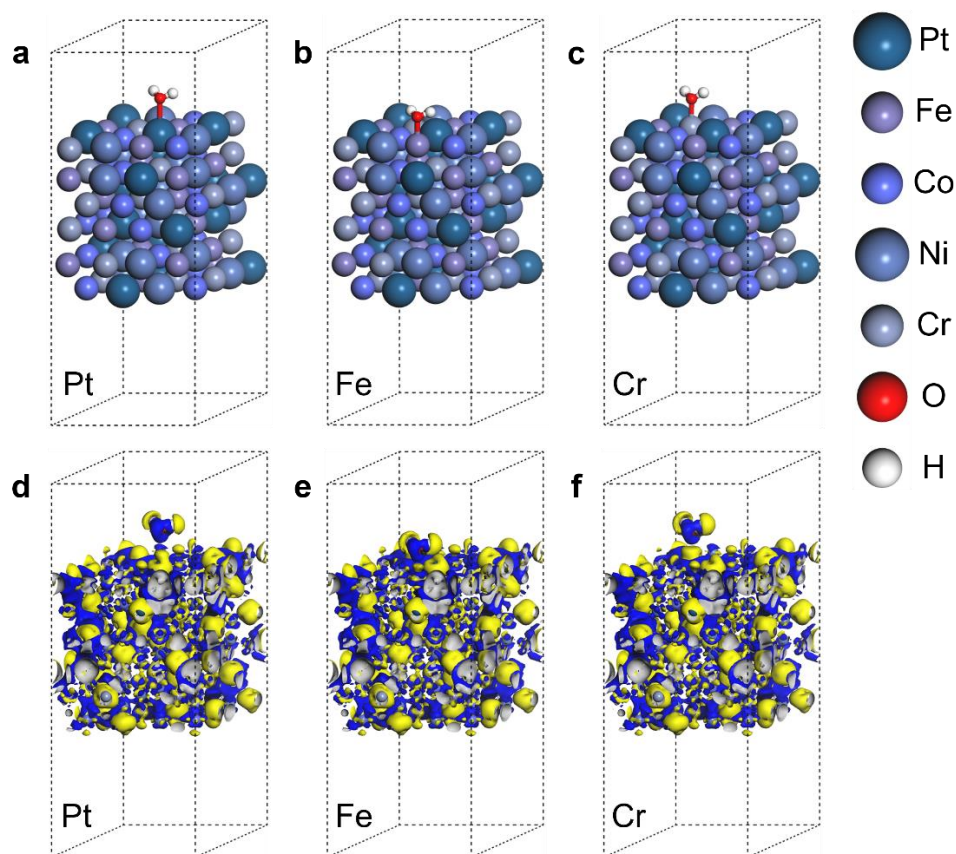


Figure S21. Atomic configurations and electron density difference analysis. DFT simulations of (a-c) atomic configurations and (d-f) electron density difference of as-dep FeCoNiCrPt after H₂O adsorption onto Pt, Fe, and Cr sites, respectively. Yellow and blue isosurfaces represent the depletion and segregation of electrons, respectively.

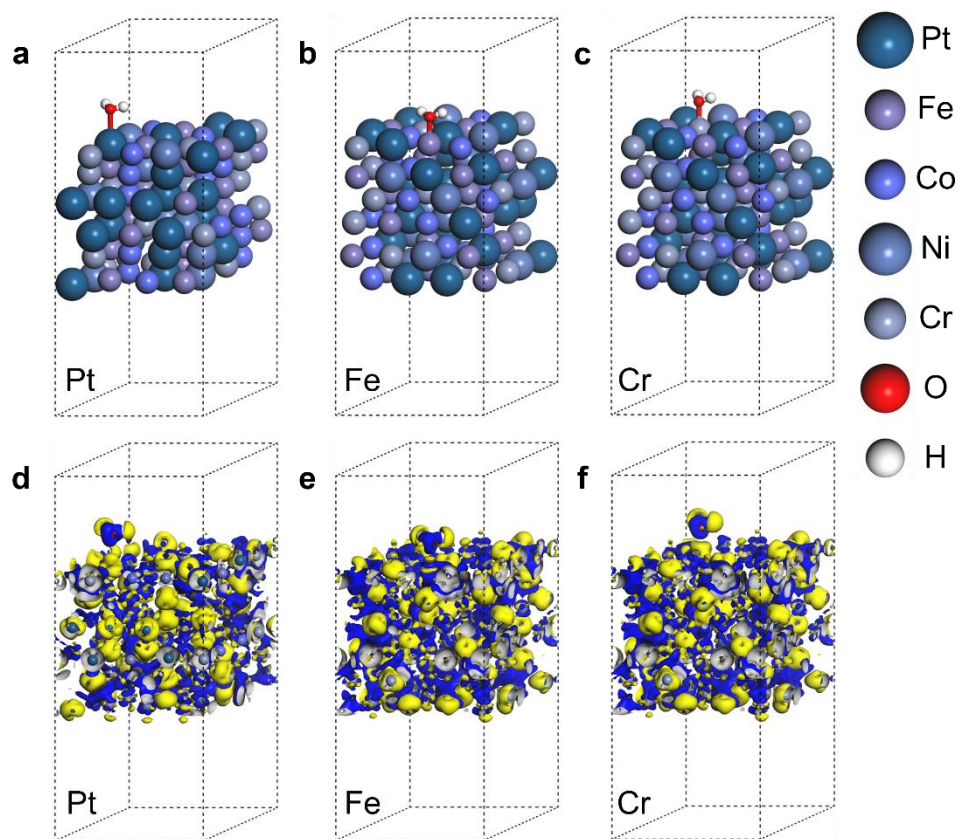


Figure S22. Atomic configurations and electron density difference analysis. DFT simulations of (a-c) atomic configurations and (d-f) electron density difference of EE.300s FeCoNiCrPt after H₂O adsorption onto Pt, Fe, and Cr sites, respectively. Yellow and blue isosurfaces represent the depletion and segregation of electrons, respectively.

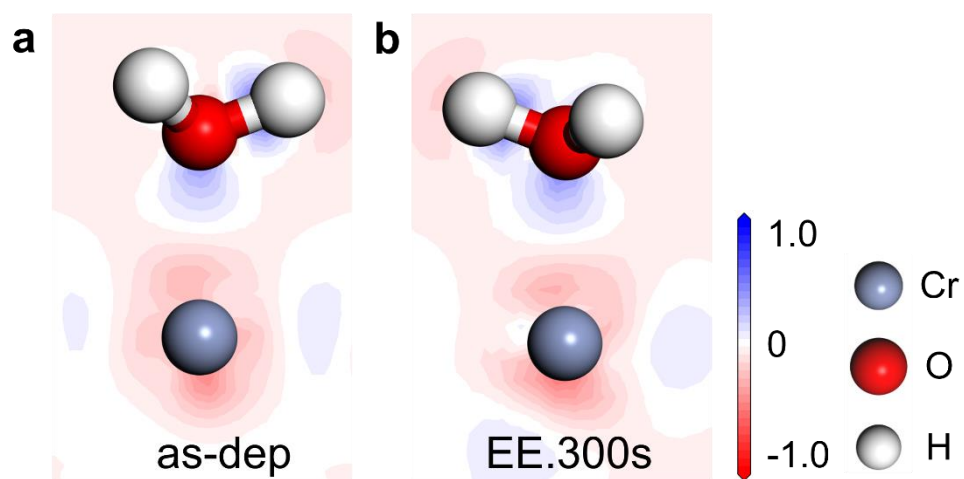


Figure S23. 2D electron density difference analysis. DFT results of 2D electron density differences after adsorption of H* onto Cr sites of the (a) as-dep and (b) EE.300s FeCoNiCrPt models, respectively. Red and blue represent the depletion and accumulation of electrons with the unit of $e/\text{\AA}^3$, respectively.

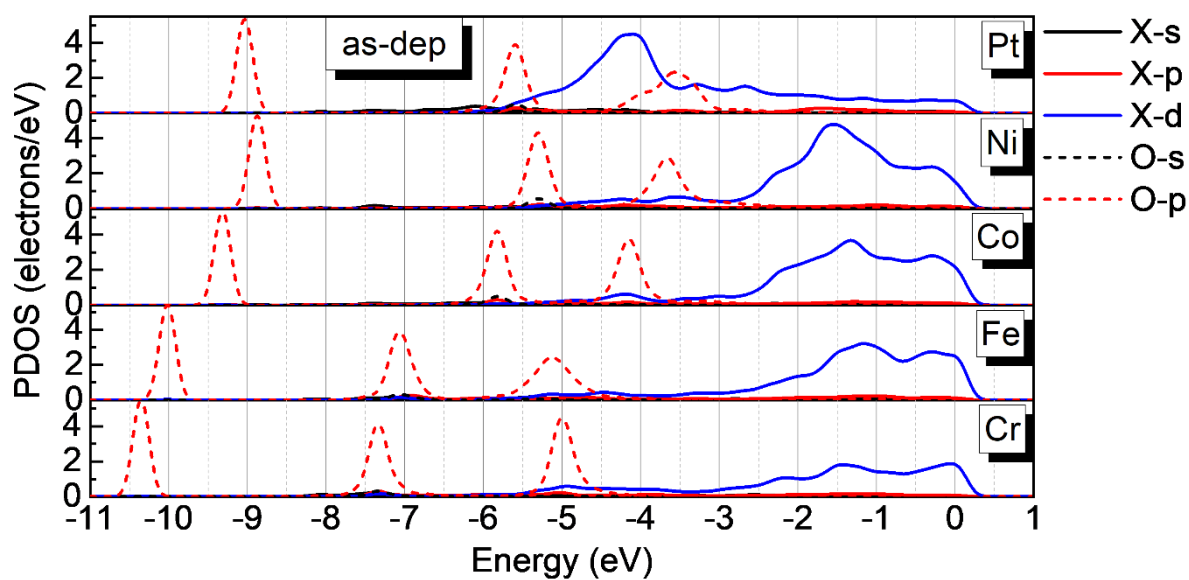


Figure S24. Partial density of states (PDOS) after H₂O adsorption onto Pt, Ni, Co, Fe, and Cr sites of the as-dep FeCoNiCrPt models. X = Pt, Ni, Co, Fe, and Cr.

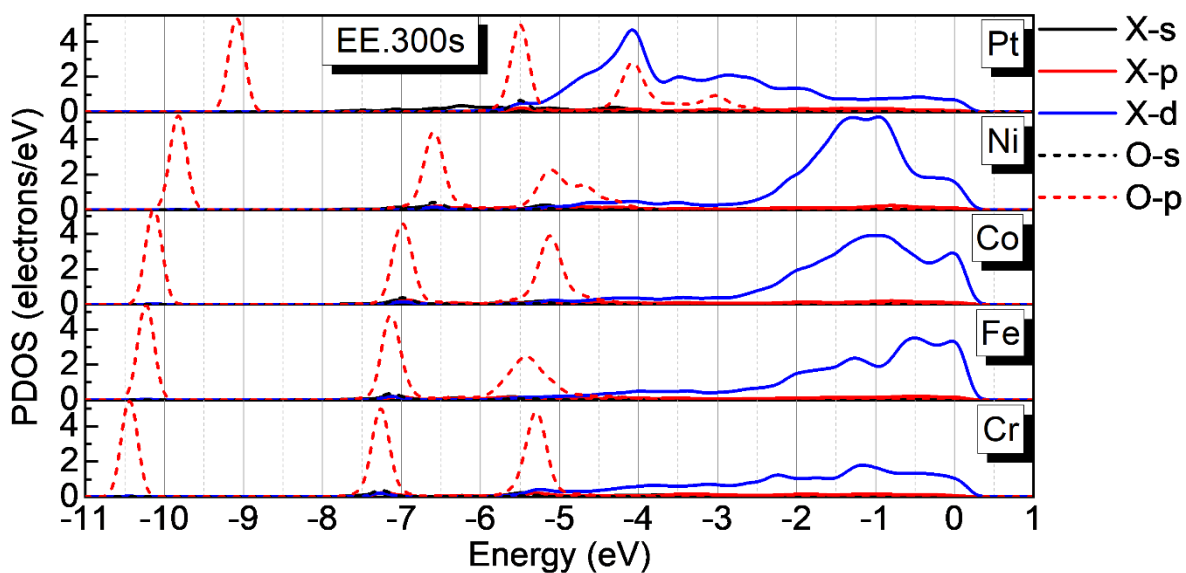


Figure S25. Partial density of states (PDOS) after H₂O adsorption onto Pt, Ni, Co, Fe, and Cr sites of the EE.300s FeCoNiCrPt models. X = Pt, Ni, Co, Fe, and Cr.

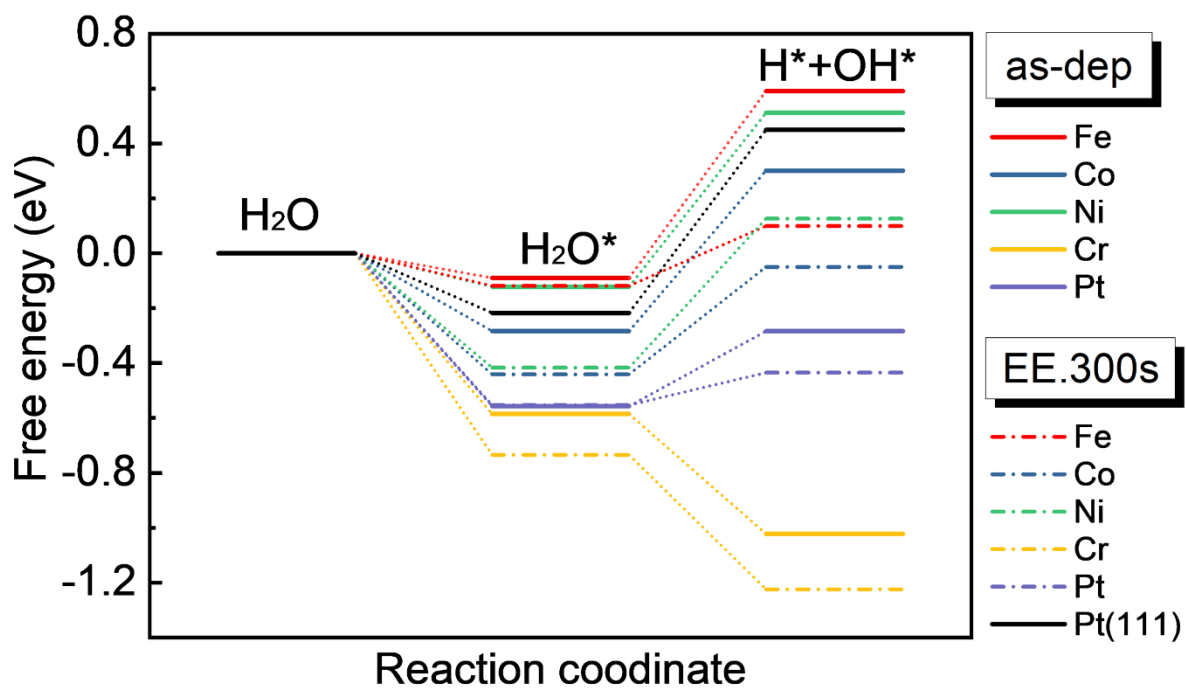


Figure S26. H_2O dissociation analysis. Free energy diagrams of reaction coordinates for H_2O dissociation on the active sites of as-dep, EE.300s, and Pt (111) models.

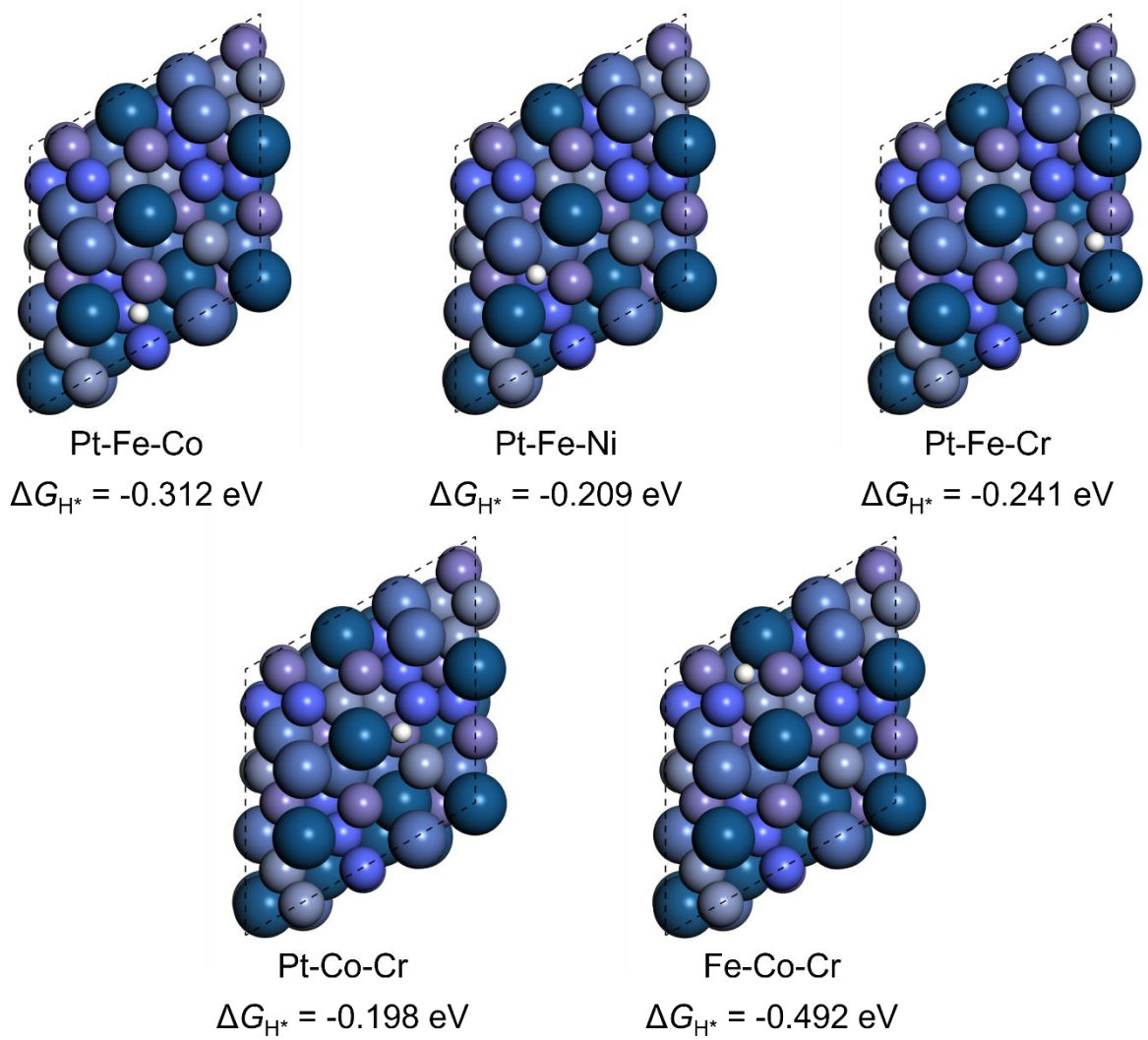


Figure S27. The representative atomic configurations with corresponding ΔG_{H^*} after H* adsorption at the triple-atom sites of the as-dep FeCoNiCrPt models.

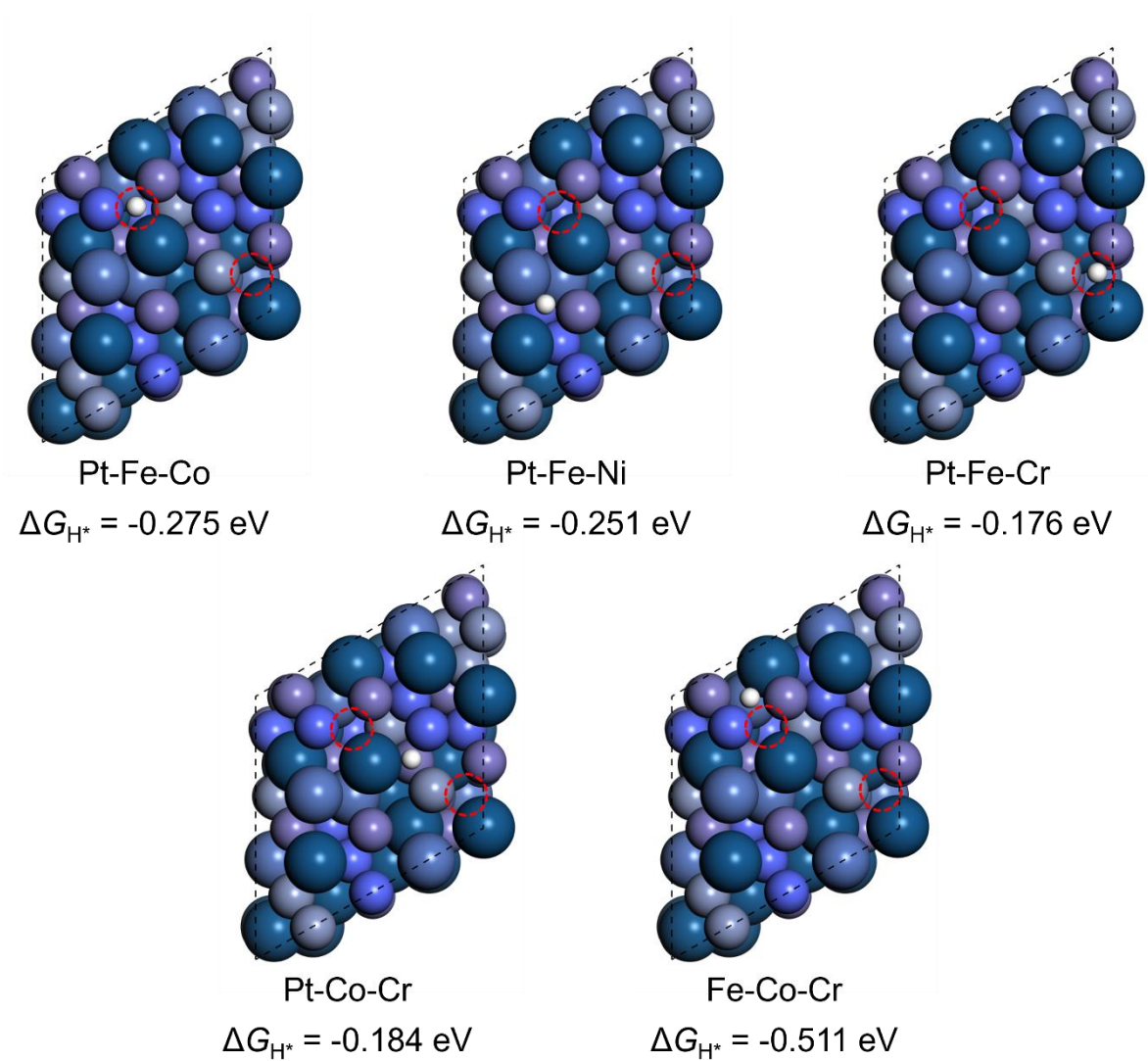


Figure S28. The representative atomic configurations with corresponding ΔG_{H^*} after H^* adsorption at the triple-atom sites of the EE.300s FeCoNiCrPt models with vacancies highlighted by red circles.

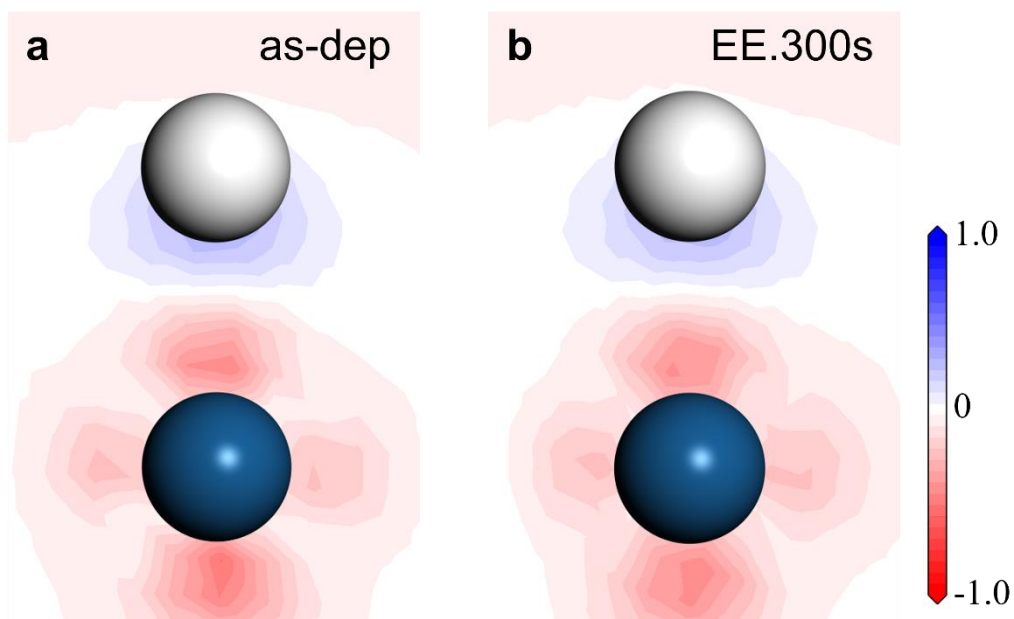


Figure S29. DFT results of 2D electron density differences after adsorption of H^* onto Pt sites of the (a) as-dep and (b) EE.300s FeCoNiCrPt models, respectively. Red and blue represent the depletion and accumulation of electrons with the unit of $e/\text{\AA}^3$, respectively.

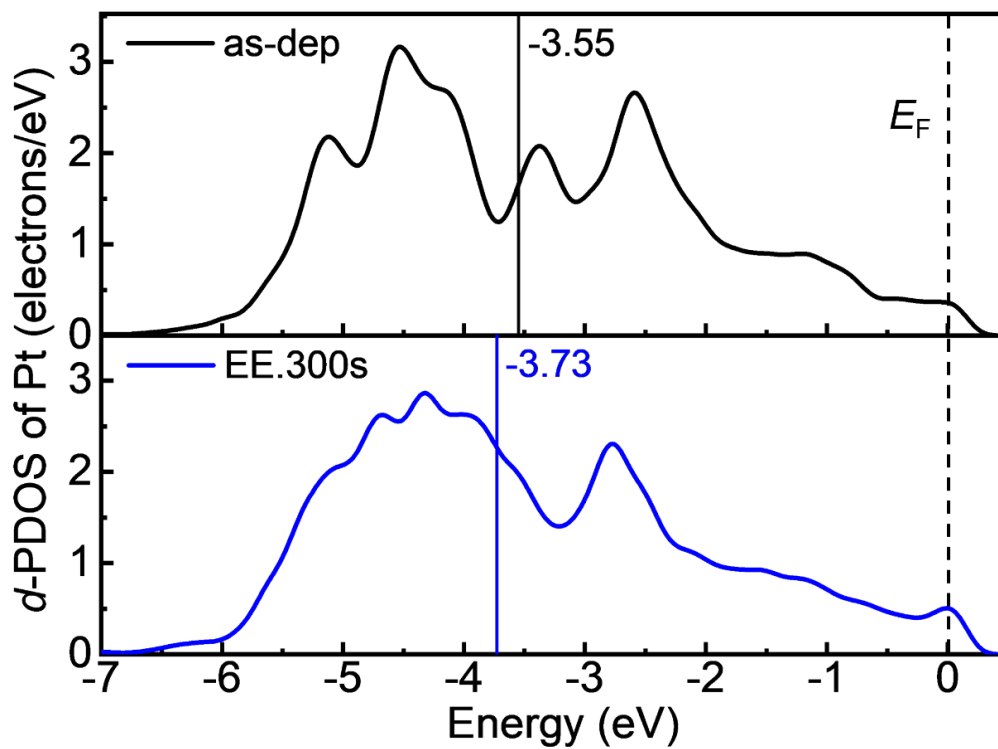


Figure S30. The d -orbital partial density of states (d -PDOS) of Pt with H^* adsorption onto the surfaces of as-dep and EE.300s FeCoNiCrPt models, respectively. The solid lines show the position of d -band centers with the values denoted and the dashed line indicates the Fermi level (E_F).

Table S1. Atomic compositions analyzed by EDS and ICP-OES for the FeCoNiCrPt films before and after electrochemical etching.

Contents (at. %)		Fe	Co	Ni	Cr	Pt
EDS	as-dep	20.7	19.9	20.4	18.8	20.2
	EE.150s	19.6	19.1	19.8	19.0	22.4
	EE.300s	23.0	18.6	14.1	18.6	25.6
	EE.800s	20.3	18.7	18.5	19.7	22.7
ICP-OES	as-dep	19.7	19.5	19.6	20.2	21.0
	EE.150s	21.0	17.2	17.1	19.5	25.2
	EE.300s	19.4	17.1	17.1	18.9	27.5
	EE.800s	21.1	16.8	16.9	18.2	27.0

Table S2. The calculated distances between two adjacent atoms based on the intensity profile in Fig. 1g.

number	1	2	3	4	5	6	7
distance(Å)	1.47	1.29	1.44	0.91	1.76	1.38	1.41
number	8	9	10	11	12	13	14
distance(Å)	1.38	1.35	1.63	1.13	1.41	1.38	1.41

Table S3. Summary of the Pt L_3 -edge XANES spectra and average valent state of Pt for as-dep and EE.300s HEA films.

Sample	Energy (eV)	Valence of Pt ^a
PtO ₂	11574.0	4
as-dep	11573.0	3.41
EE.300s	11571.7	2.65
Pt foil	11567.2	0

a: The equation: $Y = 1.7X + 11567.2$ where Y is the valence of Pt and X is the corresponding energy at the normalized intensity of 1.15 from the Pt L_3 -edge XANES spectra.

Table S4. EXAFS fitting parameters at the Pt L_3 -edge for various samples ($S_0^2=0.837$).

Sample	Shell	CN^a	$R(\text{\AA})^b$	$\sigma^2(\text{\AA}^2)^c$	$\Delta E_0(\text{eV})^d$	R factor
Pt foil	Pt-Pt	12*	2.768±0.002	0.0049±0.0002	8.7±0.7	0.0029
Pt/C	Pt-C	3.9±0.1	2.352±0.004	0.0047±0.0017	-5.0±9.4	0.0199
	Pt-Pt	9.6±0.4	3.081±0.024	0.0098±0.0013	-2.6±5.6	
as-dep	Pt-O	1.9±0.6	2.024±0.001	0.0105±0.0058	5.8±3.6	0.0051
	Pt-M [†]	3.6±0.8	2.567±0.024	0.0072±0.0028	2.2±4.1	
	Pt-Pt	1.6±0.5	3.147±0.026	0.0182±0.0054	-1.1±2.3	
EE.300s	Pt-O	1.8±0.5	2.046±0.023	0.0094±0.0038	7.4±2.4	0.0085
	Pt-M	2.9±0.6	2.588±0.014	0.0121±0.0048	-9.3±1.8	
	Pt-Pt	2.1±0.5	3.110±0.012	0.0143±0.0027	4.7±5.0	

^a CN , coordination number; ^b R , the distance to the neighboring atom; ^c σ^2 , the mean square relative displacement (MSRD); ^d ΔE_0 , inner potential correction; R factor indicates the goodness of the fit. S_0^2 was fixed to 0.837, according to the experimental EXAFS fit of Pt foil by fixing CN as the known crystallographic value. *This value was fixed during EXAFS fitting, based on the known structure of Pt. Fitting range: $3.0 \leq k (\text{\AA}^{-1}) \leq 13.2$ and $1.0 \leq R (\text{\AA}) \leq 3.0$ (Pt foil); $2.0 \leq k (\text{\AA}^{-1}) \leq 12.1$ and $1.2 \leq R (\text{\AA}) \leq 4.0$ (Pt/C); $2.0 \leq k (\text{\AA}^{-1}) \leq 10.0$ and $1.0 \leq R (\text{\AA}) \leq 4.0$ (as-dep); $1.5 \leq k (\text{\AA}^{-1}) \leq 10.5$ and $1.0 \leq R (\text{\AA}) \leq 4.0$ (EE.300s). A reasonable range of EXAFS fitting parameters: $0.700 < S_0^2 < 1.000$; $CN > 0$; $\sigma^2 > 0 \text{\AA}^2$; $|\Delta E_0| < 10 \text{ eV}$; R factor < 0.02 . [†]M represents 3d transition metals Fe, Co, Ni, and Cr.

Table S5. The comparison of HER performance of the EE.300s FeCoNiCrPt HEA film with recently reported electrocatalysts in 1.0 M KOH at current densities of 10, 100, 500, and 1000 mA cm⁻².

Catalysts	$\eta@10 \text{ mA cm}^{-2}$	Refs.
EE.300s FeCoNiCrPt	18	this work
PtSA/ α -MoC _{1-x} @C	21	10
CoNiRu	22	11
Ru@Ni-MOF	22	12
PtTe ₂	22	13
RuAu SAA	24	14
PtSA-NiO/Ni	26	15
Pd ₄ S/Pd ₃ P _{0.95}	28	16
RuCo@NCNT/PF	28	17
Pt-SAs/MoSe ₂	29	18
PtSA-Co(OH) ₂	29	19
PdPtCuNiP	32	20
Pt/MXene	34	21
NiRu _{0.13} -BDC	34	22
RuSi	37	23
PtSi	38	24
Pt/MgO	39	25
VO-Ru/HfO ₂	39	26
FeCoPdIrPt@GO	42	27
PtSe ₂ /Pt	42	28
Pt ₁ /N-C	46	29
Ni ₅ P ₄ -Ru	54	30
Sr ₂ RuO ₄	61	31
FeCoNiAlTi	88.2	32
Co(OH) ₂ /Pt	248	33
Catalysts	$\eta@100 \text{ mA cm}^{-2}$	Refs.
EE.300s FeCoNiCrPt	42	this work
PtRuRhCoNi NWs/C	60	34
Pt/MgO	105	25
PtSA/ α -MoC _{1-x} @C	117	10

Catalysts	$\eta@100 \text{ mA cm}^{-2}$	Refs.
CoNiRu	124	11
RuCo@NCNT/PF	130	17
FeCoPdIrPt@GO	135	27
Pt/MXene	185	21
Catalysts	$\eta@500 \text{ mA cm}^{-2}$	Refs.
EE.300s FeCoNiCrPt	75	this work
Ni/NiO@MoO _{3-x}	112@200 mA cm ⁻²	35
Ni-W	303	36
Pd ₄ S/Pd ₃ P _{0.95}	387	16
Catalysts	$\eta@1000 \text{ mA cm}^{-2}$	Refs.
EE.300s FeCoNiCrPt	104	this work
Fe-doped Ni ₂ P in CNT	183	37
MoC ₂ /MoS ₂	220	38
Ni ₂ P/NF	306	39
Pd ₄ S/Pd ₃ P _{0.95}	486	16

Table S6. The comparison of HER performance of the EE.300s FeCoNiCrPt HEA film with recently reported electrocatalysts in 0.5 M H₂SO₄ at current densities of 10, 100, 500, and 1000 mA cm⁻².

Catalysts	$\eta@10 \text{ mA cm}^{-2}$	Refs.
EE.300s FeCoNiCrPt	46	this work
PtSA/S-C	53	40
Ru-gCN	54.5	41
PdPtCuNiP	62	20
PtN _x /TiO ₂	67	42
PdNiCuP	76	43
SA Pt-decorated VS ₂	77	44
IrNiTa	99	4
Pt@PCM	106	45
Catalysts	$\eta@100 \text{ mA cm}^{-2}$	Refs.
EE.300s FeCoNiCrPt	64	this work
PtSA/ α -MoC _{1-x} @C	106	10
RuCo@NCNT/PF	107	17
Catalysts	$\eta@500 \text{ mA cm}^{-2}$	Refs.
EE.300s FeCoNiCrPt	87	this work
CoP HNS/CF	180	46
Pd ₄ S/Pd ₃ P _{0.95}	284	16
PtGa	113@600	47
Catalysts	$\eta@1000 \text{ mA cm}^{-2}$	Refs.
EE.300s FeCoNiCrPt	106	this work
MoC ₂ /MoS ₂	227	38
α -MoB ₂	334	48
MoS ₂ /Mo ₂ C	412	49
Pd ₄ S/Pd ₃ P _{0.95}	538	16

Table S7. The comparison of HER performance of the EE.300s FeCoNiCrPt HEA film with recently reported electrocatalysts in 1.0 M PBS at current densities of 10 and 100 mA cm⁻².

Catalysts	$\eta@10 \text{ mA cm}^{-2}$	Refs.
Ru ₂ B ₃ @BNC	58	50
PtSi	66	24
PtNi@Ti ₃ C ₂ Mxene	67	51
EE.300s FeCoNiCrPt	73	this work
PdP ₂ @CB	84.6	52
L-RuP	95	53
Ru@CN	100	54
RhCoB aerogel	113	55
Li-IrSe ₂	120	56
Co/CoP	138	57
OsP ₂ @NPC	144	58
NiS ₂ /MoS ₂	159	59
RhCu	165	60
2.20wt% Ru SAs-Ni ₂ P	260	61
NiRu@NC	482	62
Catalysts	$\eta@100 \text{ mA cm}^{-2}$	Refs.
EE.300s FeCoNiCrPt	174	this work
RuCo@NCNT/PF	187	17
Ni-SP	214	63
PSS-PPy/Ni-Co-P@50	200	64

Table S8. ICP-OES results of the electrolyte after HER stability test for 58 h at current densities of 10 and 100 mA cm⁻².

	Fe	Co	Ni	Cr	Pt
Concentration (ppm)	0.0363	0.0029	0.0043	0.0101	0.0010

Table S9. Atomic compositions analyzed by EDS for the EE.300s FeCoNiCrPt film after durability testing.

Contents (at. %)	Fe	Co	Ni	Cr	Pt	O
EE.300s	16.16	14.44	13.31	13.63	26.25	16.20

Table S10. The H₂O adsorption sites, adsorption energies ($\Delta E_{\text{H}_2\text{O}}$) and the bonding distances between active sites and the O atom in H₂O.

Model	Adsorption site	$\Delta E_{\text{H}_2\text{O}}$ (eV)	Bonding distance
as-dep EE.300s	Pt top	-0.090 -0.119	~2.714 Å ~2.710 Å
as-dep EE.300s	Fe top	-0.557 -0.583	~2.092 Å ~2.048 Å
as-dep EE.300s	Co top	-0.284 -0.442	~2.417 Å ~2.106 Å
as-dep EE.300s	Ni top	-0.122 -0.417	~2.568 Å ~2.123 Å
as-dep EE.300s	Cr top	-0.586 -0.734	~2.157 Å ~2.139 Å

Table S11. The H* Gibbs free energy (ΔG_{H^*}) for various active sites in the as-dep and EE.300s FeCoNiCrPt film.

Active site		ΔG_{H^*} (eV)
Pt	Pt(111)	-0.10685
as-dep	Pt-Fe-Co	-0.31163
	Pt-Fe-Ni	-0.20939
	Pt-Fe-Cr	-0.24124
	Pt-Co-Cr	-0.19787
	Fe-Co-Cr	-0.49157
	Pt	-0.13035
EE.300s	Pt-Fe-Co	-0.27476
	Pt-Fe-Ni	-0.25125
	Pt-Fe-Cr	-0.17581
	Pt-Co-Cr	-0.18388
	Fe-Co-Cr	-0.51067
	Pt	0.02301

References

- 1 B. Ravel and M. Newville, *J. Synchrotron. Radiat.*, 2005, **12**, 537-541.
- 2 S. I. Zabinsky, J. J. Rehr, A. Ankudinov, R. C. Albers and M. J. Eller, *Phys. Rev. B Condens. Matter.*, 1995, **52**, 2995-3009.
- 3 Z. Xia, H. Zhang, K. Shen, Y. Qu and Z. Jiang, *Physica B Condens. Matter.*, 2018, **542**, 12-19.
- 4 Z. J. Wang, M. X. Li, J. H. Yu, X. B. Ge, Y. H. Liu and W. H. Wang, *Adv. Mater.*, 2020, **32**, e1906384.
- 5 W. M. Haynes, D. R. Lide and T. J. Bruno, *CRC Handbook of Chemistry and Physics*.
- 6 S. J. Clark, M. D. Segall, C. J. Pickard, P. J. Hasnip, M. I. J. Probert, K. Refson and M. C. Payne, *Z. Krist.-Cryst. Mater.*, 2005, **220**, 567-570.
- 7 J. P. Perdew, K. Burke and M. Ernzerhof, *Phys. Rev. Lett.*, 1996, **77**, 2865-2868.
- 8 D. Vanderbilt, *Phys. Rev. B Condens. Matter.*, 1990, **41**, 7892-7895.
- 9 H. J. Monkhorst and J. D. Pack, *Phys. Rev. B*, 1976, **13**, 5188-5192.
- 10 W. Wang, Y. Wu, Y. Lin, J. Yao, X. Wu, C. Wu, X. Zuo, Q. Yang, B. Ge, L. Yang, G. Li, S. Chou, W. Li and Y. Jiang, *Adv. Funct. Mater.*, 2021, **32**, 2108464.
- 11 Y. Wang, S. Wang, Z. L. Ma, L. T. Yan, X. B. Zhao, Y. Y. Xue, J. M. Huo, X. Yuan, S. N. Li and Q. G. Zhai, *Adv. Mater.*, 2022, **34**, e2107488.
- 12 L. Deng, F. Hu, M. Ma, S. C. Huang, Y. Xiong, H. Y. Chen, L. Li and S. Peng, *Angew. Chem. Int. Ed.*, 2021, **60**, 22276-22282.
- 13 X. Li, Y. Fang, J. Wang, H. Fang, S. Xi, X. Zhao, D. Xu, H. Xu, W. Yu, X. Hai, C. Chen, C. Yao, H. B. Tao, A. G. R. Howe, S. J. Pennycook, B. Liu, J. Lu and C. Su, *Nat. Commun.*, 2021, **12**, 2351.
- 14 C. H. Chen, D. Wu, Z. Li, R. Zhang, C. G. Kuai, X. R. Zhao, C. K. Dong, S. Z. Qiao, H. Liu and X. W. Du, *Adv. Energy Mater.*, 2019, **9**, 1803913.
- 15 K. L. Zhou, Z. Wang, C. B. Han, X. Ke, C. Wang, Y. Jin, Q. Zhang, J. Liu, H. Wang and H. Yan, *Nat. Commun.*, 2021, **12**, 3783.
- 16 G. Zhang, A. Wang, L. Niu, W. Gao, W. Hu, Z. Liu, R. Wang and J. Chen, *Adv. Energy Mater.*, 2022, **12**, 2103511.
- 17 J. Jiao, N. N. Zhang, C. Zhang, N. Sun, Y. Pan, C. Chen, J. Li, M. Tan, R. Cui, Z. Shi, J. Zhang, H. Xiao and T. Lu, *Adv. Sci.*, 2022, **9**, e2200010.
- 18 Y. Shi, Z. R. Ma, Y. Y. Xiao, Y. C. Yin, W. M. Huang, Z. C. Huang, Y. Z. Zheng, F. Y. Mu, R. Huang, G. Y. Shi, Y. Y. Sun, X. H. Xia and W. Chen, *Nat. Commun.*, 2021, **12**, 3021.
- 19 K. L. Zhou, C. Wang, Z. Wang, C. B. Han, Q. Zhang, X. Ke, J. Liu and H. Wang, *Energy Environ. Sci.*, 2020, **13**, 3082-3092.
- 20 Z. Jia, K. Nomoto, Q. Wang, C. Kong, L. Sun, L. C. Zhang, S. X. Liang, J. Lu and J. J. Kruzic, *Adv. Funct. Mater.*, 2021, **31**, 2101586.
- 21 Y. Wu, W. Wei, R. Yu, L. Xia, X. Hong, J. Zhu, J. Li, L. Lv, W. Chen, Y. Zhao, L. Zhou and L. Mai, *Adv. Funct. Mater.*, 2022, **32**, 2110910.
- 22 Y. Sun, Z. Xue, Q. Liu, Y. Jia, Y. Li, K. Liu, Y. Lin, M. Liu, G. Li and C. Y. Su, *Nat. Commun.*, 2021, **12**, 1369.
- 23 H. Chen, X. Ai, W. Liu, Z. Xie, W. Feng, W. Chen and X. Zou, *Angew. Chem. Int. Ed.*, 2019, **58**, 11409-11413.
- 24 Z. Pu, T. Liu, G. Zhang, Z. Chen, D. S. Li, N. Chen, W. Chen, Z. Chen and S. Sun, *Adv. Energy Mater.*, 2022, **12**, 2200293.
- 25 H. Tan, B. Tang, Y. Lu, Q. Ji, L. Lv, H. Duan, N. Li, Y. Wang, S. Feng, Z. Li, C. Wang, F. Hu, Z. Sun and W. Yan, *Nat. Commun.*, 2022, **13**, 2024.
- 26 G. Li, H. Jang, S. Liu, Z. Li, M. G. Kim, Q. Qin, X. Liu and J. Cho, *Nat. Commun.*, 2022, **13**, 1270.
- 27 S. Gao, S. Hao, Z. Huang, Y. Yuan, S. Han, L. Lei, X. Zhang, R. Shahbazian-Yassar and J. Lu, *Nat. Commun.*, 2020, **11**, 2016.

- 28 Z. Wang, B. Xiao, Z. Lin, Y. Xu, Y. Lin, F. Meng, Q. Zhang, L. Gu, B. Fang, S. Guo and W. Zhong, *Angew. Chem. Int. Ed.*, 2021, **60**, 23388-23393.
- 29 S. Fang, X. Zhu, X. Liu, J. Gu, W. Liu, D. Wang, W. Zhang, Y. Lin, J. Lu, S. Wei, Y. Li and T. Yao, *Nat. Commun.*, 2020, **11**, 1029.
- 30 Q. He, D. Tian, H. Jiang, D. Cao, S. Wei, D. Liu, P. Song, Y. Lin and L. Song, *Adv. Mater.*, 2020, **32**, e1906972.
- 31 Y. Zhu, H. A. Tahini, Z. Hu, J. Dai, Y. Chen, H. Sun, W. Zhou, M. Liu, S. C. Smith, H. Wang and Z. Shao, *Nat. Commun.*, 2019, **10**, 149.
- 32 Z. Jia, T. Yang, L. Sun, Y. Zhao, W. Li, J. Luan, F. Lyu, L. C. Zhang, J. J. Kruzic, J. J. Kai, J. C. Huang, J. Lu and C. T. Liu, *Adv. Mater.*, 2020, **32**, 2000385.
- 33 R. Subbaraman, D. Tripkovic, K. C. Chang, D. Strmcnik, A. P. Paulikas, P. Hirunsit, M. Chan, J. Greeley, V. Stamenkovic and N. M. Markovic, *Nat. Mater.*, 2012, **11**, 550-557.
- 34 H. Li, M. Sun, Y. Pan, J. Xiong, H. Du, Y. Yu, S. Feng, Z. Li, J. Lai, B. Huang and L. Wang, *Appl. Catal. B*, 2022, **312**, 121431.
- 35 J. Y. Zhang, J. Liang, B. Mei, K. Lan, L. Zu, T. Zhao, Y. Ma, Y. Chen, Z. Lv, Y. Yang, C. Yu, Z. Xu, B. Y. Xia, W. Li, Q. Yuan and D. Zhao, *Adv. Energy Mater.*, 2022, **12**, 2200001.
- 36 H. Wu, L. Kong, Y. Ji, J. Yan, Y. Ding, Y. Li, S. T. Lee and S. Liu, *Adv. Mater. Interfaces*, 2019, **6**, 1900308.
- 37 H. Sun, Y. Min, W. Yang, Y. Lian, L. Lin, K. Feng, Z. Deng, M. Chen, J. Zhong, L. Xu and Y. Peng, *ACS Catal.*, 2019, **9**, 8882-8892.
- 38 Y. Luo, L. Tang, U. Khan, Q. Yu, H. M. Cheng, X. Zou and B. Liu, *Nat. Commun.*, 2019, **10**, 269.
- 39 X. Yu, Z. Y. Yu, X. L. Zhang, Y. R. Zheng, Y. Duan, Q. Gao, R. Wu, B. Sun, M. R. Gao, G. Wang and S. H. Yu, *J. Am. Chem. Soc.*, 2019, **141**, 7537-7543.
- 40 Q. Q. Yan, D. X. Wu, S. Q. Chu, Z. Q. Chen, Y. Lin, M. X. Chen, J. Zhang, X. J. Wu and H. W. Liang, *Nat. Commun.*, 2019, **10**, 4977.
- 41 Z. Yu, Y. Li, A. Torres-Pinto, A. P. LaGrow, V. M. Diaconescu, L. Simonelli, M. J. Sampaio, O. Bondarchuk, I. Amorim, A. Araujo, A. M. T. Silva, C. G. Silva, J. L. Faria and L. Liu, *Appl. Catal. B*, 2022, **310**, 121318.
- 42 X. Cheng, Y. Lu, L. Zheng, Y. Cui, M. Niibe, T. Tokushima, H. Li, Y. Zhang, G. Chen, S. Sun and J. Zhang, *Nano Energy*, 2020, **73**, 104739.
- 43 Y. C. Hu, Y. Z. Wang, R. Su, C. R. Cao, F. Li, C. W. Sun, Y. Yang, P. F. Guan, D. W. Ding, Z. L. Wang and W. H. Wang, *Adv. Mater.*, 2016, **28**, 10293-10297.
- 44 J. Zhu, L. Cai, X. Yin, Z. Wang, L. Zhang, H. Ma, Y. Ke, Y. Du, S. Xi, A. T. S. Wee, Y. Chai and W. Zhang, *ACS Nano*, 2020, **14**, 5600-5608.
- 45 Huabin Zhang, Pengfei An, Wei Zhou, Bu Yuan Guan, Peng Zhang, Juncai Dong and X. W. D. Lou, *Sci. Adv.*, 2018, **4**, eaao6657.
- 46 H. Yoon, H. J. Song, B. Ju and D.-W. Kim, *Nano Res.*, 2020, **13**, 2469-2477.
- 47 Q. Yang, G. Li, K. Manna, F. Fan, C. Felser and Y. Sun, *Adv. Mater.*, 2020, **32**, e1908518.
- 48 Y. Chen, G. Yu, W. Chen, Y. Liu, G. D. Li, P. Zhu, Q. Tao, Q. Li, J. Liu, X. Shen, H. Li, X. Huang, D. Wang, T. Asefa and X. Zou, *J. Am. Chem. Soc.*, 2017, **139**, 12370-12373.
- 49 C. Zhang, Y. Luo, J. Tan, Q. Yu, F. Yang, Z. Zhang, L. Yang, H. M. Cheng and B. Liu, *Nat. Commun.*, 2020, **11**, 3724.
- 50 Y. Qiao, P. Yuan, C.-W. Pao, Y. Cheng, Z. Pu, Q. Xu, S. Mu and J. Zhang, *Nano Energy*, 2020, **75**, 104881.
- 51 Y. Yan, R. Zhang, Y. Yu, Z. Sun, R. Che, B. Wei, A. P. LaGrow, Z. Wang and W. Zhou, *Appl. Catal. B*, 2021, **291**, 120100.
- 52 F. Luo, Q. Zhang, X. Yu, S. Xiao, Y. Ling, H. Hu, L. Guo, Z. Yang, L. Huang, W. Cai and H. Cheng, *Angew. Chem. Int. Ed.*, 2018, **57**, 14862-14867.
- 53 J. Yu, Y. Guo, S. She, S. Miao, M. Ni, W. Zhou, M. Liu and Z. Shao, *Adv. Mater.*, 2018, **30**, e1800047.

- 54 J. Wang, Z. Wei, S. Mao, H. Li and Y. Wang, *Energy Environ. Sci.*, 2018, **11**, 800-806.
- 55 K. Deng, T. Ren, Y. Xu, S. Liu, Z. Dai, Z. Wang, X. Li, L. Wang and H. Wang, *J. Mater. Chem. A*, 2020, **8**, 5595-5600.
- 56 T. Zheng, C. Shang, Z. He, X. Wang, C. Cao, H. Li, R. Si, B. Pan, S. Zhou and J. Zeng, *Angew. Chem. Int. Ed.*, 2019, **58**, 14764-14769.
- 57 Z.-H. Xue, H. Su, Q.-Y. Yu, B. Zhang, H.-H. Wang, X.-H. Li and J.-S. Chen, *Adv. Energy Mater.*, 2017, **7**, 1602355.
- 58 S. Chakrabarty, B. K. Barman and C. Retna Raj, *Chem. Commun.*, 2019, **55**, 4399-4402.
- 59 P.-F. Cheng, T. Feng, Z.-W. Liu, D.-Y. Wu and J. Yang, *Chinese J. Catal.*, 2019, **40**, 1147-1152.
- 60 D. Cao, H. Xu and D. Cheng, *Adv. Energy Mater.*, 2020, **10**, 1903038.
- 61 K. Wu, K. Sun, S. Liu, W.-C. Cheong, Z. Chen, C. Zhang, Y. Pan, Y. Cheng, Z. Zhuang, X. Wei, Y. Wang, L. Zheng, Q. Zhang, D. Wang, Q. Peng, C. Chen and Y. Li, *Nano Energy*, 2021, **80**, 105467.
- 62 Y. Xu, S. Yin, C. Li, K. Deng, H. Xue, X. Li, H. Wang and L. Wang, *J. Mater. Chem. A*, 2018, **6**, 1376-1381.
- 63 M. I. Abdullah, A. Hameed, N. Zhang and M. Ma, *ChemElectroChem*, 2019, **6**, 2100-2106.
- 64 F. Tian, S. Geng, L. He, Y. Huang, A. Fauzi, W. Yang, Y. Liu and Y. Yu, *Chem. Eng. J.*, 2021, **417**, 129232.